Solid State Communications 150 (2010) 1023–1039

Contents lists available at ScienceDirect

Solid State Communications

journal homepage: www.elsevier.com/locate/ssc

Electrorheology: Statics and dynamics

Ping Sheng*, Weijia Wen

Department of Physics, Hong Kong University of Science & Technology, Clear Water Bay, Kowloon, Hong Kong, China

ARTICLE INFO

Article history:
Received 1 September 2009
Accepted 11 November 2009
by the Guest Editors
Available online 18 January 2010

Keywords:
D. Mechanical properties
D. Elasticity
D. Dielectric response

ABSTRACT

The interaction between nanoparticles and an electric field is explored from the electrorheological (ER) point of view, using variational formulations for both the static and dynamic characteristics. In the first part the static characteristics of the ER fluid, consisting of a dispersion of solid particles in a liquid, is detailed by using the spectral representation approach for the effective dielectric constant. Predictions concerning the ground state structure, yield stress, upper bounds on the ER effect are presented together with comparisons to experimental results. The giant ER effect, involving a different paradigm of permanent electric dipoles, is described phenomenologically. In the second part the ER fluid dynamics is formulated via the variational principle of Onsager. Predictions of the model are compared with experiments. It is shown that the phenomenon of the diminishing ER effect at high shear rates may be mitigated by the planar interdigital electrode configuration.

1. Introduction

Consider a dispersion of particles in a fluid medium in which the particles are nano-sized or otherwise. The particles and the fluid are electrically non-conducting or slightly conducting. The latter criterion will be better defined later. When an electric field $\vec{E}$ is applied to such a colloidal dispersion, the particles will be polarized electrically. Let ε_s denote the complex dielectric constant of the solid particles and ε_ℓ that of the liquid; then for spherically shaped particles, which will be the particle shape considered in this article, the induced dipole moment may be expressed as

$$\vec{p} = \frac{\varepsilon_s - \varepsilon_\ell}{\varepsilon_s + 2\varepsilon_\ell} a^3 \vec{E} = \beta a^3 \vec{E}, \qquad (1)$$

where a is the radius of the particles. Here $\vec{E}$ should be understood as the field at the location of the particle. The resulting (induced) dipole–dipole interaction between the particles means that the random dispersion is not the lowest energy state of the system, and particles would tend to aggregate and form chains/columns along the applied field direction. The formation of chains/columns is the reason why such colloids exhibit an increased viscosity or even solid-like behavior when sheared in a direction perpendicular to the electric field. Such rheological variation is denoted the *electrorheological effect*, or ER effect. The colloids which exhibit significant ER effect are denoted electrorheological fluids, or ER fluids. The formation of chains/columns is governed by the competition between electrical energy and entropy of the particles, which is manifest in the value of the dimensionless parameter $\gamma = \vec{p} \cdot \vec{E}/k_B T$, where k_B is the Boltzmann constant and T the temperature. For room temperature and $\vec{p}$ given by Eq. (1), $\gamma = 1$ defines the boundary between the entropy-dominated regime and the ER regime. The resulting relation between the electric field and the effective size of the particle, given by $(\beta a^3)^{1/3}$, is shown in Fig. 1.

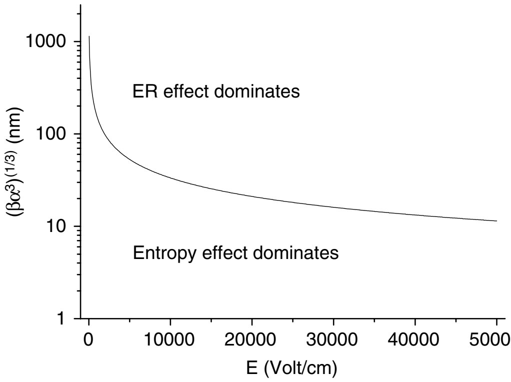

Fig. 1. A plot of the curve $\gamma = \vec{p} \cdot \vec{E}/k_B T = 1$, above which the ER effect dominates and below which the entropy effect dominates.

In what follows, we will mostly be concerned with the ER regime, where the electrical energy dominates. In Fig. 2 we show that in the ER regime, the particles tend to form chains in a weak field and columns in a strong field. In most practical systems, the highest electric field one can apply before electrical breakdown is of the order of 50 kV/cm. Hence we are limited to particles with $\beta^{1/3} a \geq 10$ nm.

---

* Corresponding author. Tel.: +852 2358 7474; fax: +852 2358 1652.
E-mail address: sheng@ust.hk (P. Sheng).

0038-1098/$ – see front matter © 2010 Elsevier Ltd. All rights reserved.
doi:10.1016/j.ssc.2010.01.020

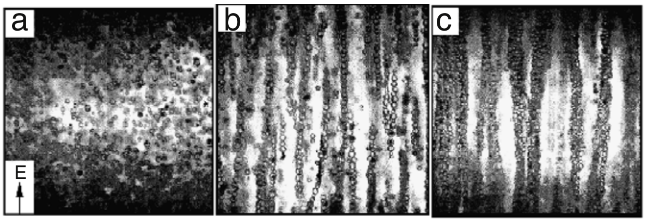

Fig. 2. The structural evolution of dielectric microspheres under an increasing electric field, from (a) no field, to (b) a moderate field of 500 V mm^{-1}, to (c) a strong field of 900 V mm^{-1}. Here the ER fluid consists of 1.5 micron glass spheres suspended in silicone oil.

1.1. History of the ER effect and its potential applications

As described above, the ER colloids are capable of viscosity variation or even solidification in response to an applied electric field. The rheological variation is reversible when the field is removed. The response time can be as short as a few milliseconds. Due to such marvelous features, the ER fluids can serve as an electric–mechanical interface; and when they are coupled with sensors (as triggers to activate the electric field), many mechanical devices such as clutches, valves, dampers etc may be converted into active mechanical elements capable of responding to environmental variations — hence ER fluids are sometimes denoted as a type of "smart" fluid. The diverse applications potential has made ER fluids a persistent area of study ever since its discovery six decades ago by Winslow [1–3]. However, during the period between its discovery in the late 1940s and the early 1980s, the ER effect was mainly a subject of scientific curiosity. It was not until the 1980s that serious research efforts were mounted, fueled in part by its potential for applications [4–10]. There have always been two sides to the ER research efforts. On one side is the basic research looking into the ER mechanism(s), and on the other are the attempts to realize the active mechanical devices. The peak of ER research occurred in late 1980s and early 1990s, but waned afterwards owing to the lack of progress on the material side of the research. In particular, the "solidification" of the ER fluids under a strong electric field, characterizable by a yield stress, can at most reach something comparable to hard "tofu," which is not sufficient for most engineering applications. But research into the basic mechanism(s) of the ER effect persisted [11–19]. More recently, however, the discovery of the "giant" ER effect [20–22], in nanoparticles of barium titanyl oxalate coated with urea, together with the appeal in the basic science of nanoparticles and their dynamics, have renewed interest in this area.

1.2. Outline

This review article is conveniently divided into a part involving the static structure of the ER fluids and its rheological characteristics, and a part on the electrorheological fluid dynamics. In the first part, a brief review of the conventional ER mechanism and the conceptual advance that made its quantitative modeling possible are given in Section 2. In particular, the variational formulation of the approach and the attendant implementation using the Bergman–Milton representation theory of the effective dielectric constant are detailed. Comparisons with experiments, in particular the ground state structure(s), the yield stress, the upper bound and its variation with particle size, and the nonlinearity and anisotropy of the effective dielectric constant, are detailed in Section 3 together with an explanation of their physical underpinnings. The motivation and discovery of the giant ER effect are presented in Section 4, together with a phenomenological theory for its mechanism.

In the second part, ER fluid dynamics will be addressed from the continuum hydrodynamic point of view. The Onsager variational principle and its statistical mechanic underpinnings will first be briefly introduced in Section 5, followed by the formulation of the two-phase modelling approach and the derivation of the relevant equations of motion in Section 6. Numerical implementation and predictions of the model are described in Section 7, together with the resolution of the shear-thinning behavior commonly observed in ER fluids at high shear rates.

2. Mechanism of the electrorheological effect

A heuristic explanation of the ER effect has been given in the previous section. However, such a simple picture leaves many questions unanswered. In particular, as the particles aggregate and touch, multipole interactions (those beyond the dipole interaction) necessarily become dominant, and the local field effect must also be taken into account. In addition, the conductivity and/or relaxational effects, appearing as the imaginary part of the particle and/or fluid dielectric constants, may contribute to the ER effect. These complications make the direct simulation of the ER effect quite difficult, and their characteristics beyond the realm of accurate prediction. In particular, for applications it is desirable to have an upper bound on the ER effect, so that devices may be designed accordingly.

2.1. Variational formulation

The conceptual advance that made the quantitative modeling of ER effect possible is the variational formulation [13,19] and description of the ER characteristics, i.e., the ground state microstructure of the solid microparticles under a high electric field, and its relevant stress–strain relation.

The variational principle is cast in terms of the Gibbs free energy density f:

$$f = -\frac{1}{8\pi}\vec{E}\cdot\mathrm{Re}(\tilde{\varepsilon}_{eff})\cdot\vec{E} - TS = -\frac{1}{8\pi}\mathrm{Re}(\bar{\varepsilon}_{zz})E^2 - TS. \tag{2}$$

Here S denotes entropy, Re() means taking the real part of the quantity in the parenthesis, and the effective dielectric constant tensor $\tilde{\varepsilon}_{eff}$ is defined and given by

$$\vec{D} = \tilde{\varepsilon}_{eff}\vec{E}, \tag{3a}$$

$$\tilde{\varepsilon}_{eff} = \begin{pmatrix} \bar{\varepsilon}_{xx} & \bar{\varepsilon}_{xy} & \bar{\varepsilon}_{xz} \\ \bar{\varepsilon}_{yx} & \bar{\varepsilon}_{yy} & \bar{\varepsilon}_{yz} \\ \bar{\varepsilon}_{zx} & \bar{\varepsilon}_{zy} & \bar{\varepsilon}_{zz} \end{pmatrix}, \tag{3b}$$

where $\vec{D}$ denotes the displacement field, $\vec{E}$ the electric field (assumed to be along the z direction), and the matrix elements of $\tilde{\varepsilon}_{eff}$ are complex in general (in the form of $\kappa + \mathrm{i}(4\pi\sigma/\omega)$, with σ being the conductivity and ω the angular frequency of the applied electric field).

The effective dielectric constant concept is based on the nature of electromagnetic wave interaction with inhomogeneous materials. When the frequency of the electromagnetic wave is sufficiently low so that its relevant wavelength is much larger than the scale of the inhomogeneities, microstructure can no longer be resolved, and the (fluid–solid) composite appears homogeneous to the probing wave. In that limit the electromagnetic response is fully captured by the effective dielectric constant tensor, which would simplify to an effective dielectric constant when the material is isotropic [23].

It should probably be noted that a strictly DC electric field is often experimentally not advisable. This is because owing to the small conductivities that may exist in either the solid particles or the liquid, or both, there is a time constant τ that is inversely proportional to the conductivities. A DC electric field will be screened by the ions at time $t > \tau$. Hence a low frequency electric field is generally applied so as to avoid screening, which does not detract from the fact that the system is still in the long wavelength limit.

An important element of the variational formulation is that the magnitudes of the matrix elements in the effective dielectric constant tensor are dependent on the relative volume fraction(s) of the constituents, as well as the anisotropy and the microstructure. This aspect enables us to link the free energy density, which is to be minimized, directly to the microstructure. Hence one can determine the ground state structure in the high field limit (so that the entropy term can be neglected) by minimizing the free energy with respect to the microstructure. In particular, one wants to maximize the (real part of the) *zz* component of the effective dielectric constant matrix elements through microstructural adjustments, as stipulated by Eq. (2).

By focusing on the ER regime, we assume that the electrical part of the free energy is much larger than the entropy part, and the second term on the right hand side of Eq. (2) is thereby ignored. In order to find the ground state microstructure explicitly, we assume that the system consists of equal-sized solid microspheres, and note that the ground state must have a periodic structure, since it is unique. Provided that the ground state can be found, the shear modulus and the yield stress may be obtained from the ground state microstructure by defining a local shear distortion and calculating the free energy difference from the ground state. The yield stress, if there is one, is defined by the maximum point of the shear stress vs. shear strain plot, beyond which the shear stress decreases with increasing strain, implying instability.

The advantage of the variational approach is that it solves, in one step, all the difficulties posed earlier. In particular, the local field effect and the multipole interactions are all accounted for, provided the effective dielectric constant can be accurately evaluated. In addition, the contribution of the imaginary part of the dielectric constant may also be incorporated through the imaginary parts of the components' dielectric constants.

2.2. Effective dielectric constant — the Bergman–Milton spectral representation

Since the essence of calculating the free energy lies in the evaluation of the effective dielectric constant, a rigorous approach to the evaluation of ε_{zz} is desirable. This is because we want to distinguish the energies of different microstructures for the (equal-sized) microspheres, e.g., body centered tetragonal (BCT) structure versus the face centered cubic (FCC) structure. These differences can be quite small and would not show up in the usual effective medium theories. In fact, the small differences between the different microstructures are manifest only at high filling fractions of the microspheres, since in that limit there can be differences in the local environments for the different periodic structures. The Bergman–Milton spectral function representation [24–28] of the effective dielectric constant provides the perfect approach to distinguish the structures from the value of $\bar{\varepsilon}_{zz}$. The starting point of its derivation is the Laplace equation

$$\nabla \cdot (\varepsilon(\vec{r})\nabla\varphi(\vec{r})) = 0. \tag{4}$$

Here φ is the electrical potential, i.e., $\vec{E} = -\nabla\varphi$, and $\varepsilon(\vec{r})$ is the local dielectric constant, given by

$$\varepsilon(\vec{r}) = \varepsilon_\ell \left(1 - \frac{1}{s}\eta(\vec{r})\right), \tag{5a}$$

where

$$s = \frac{\varepsilon_\ell}{\varepsilon_\ell - \varepsilon_s}, \tag{5b}$$

ε_ℓ denotes the liquid dielectric constant and ε_s the solid dielectric constant. Here η is the characteristic function, defined to be 1 inside the solid particles and zero elsewhere. The microgeometric information of the system are contained in η. In contrast, the parameter s (which can be complex) contains the material characteristics. For later developments it is important to note that if the dielectric constants are real, then the value of s is either greater than 1 or less than zero. In other words, a real s can not take any value between 0 and 1.

By rewriting Eqs. (4) and (5) as

$$\nabla^2\varphi(\vec{r}) = \frac{1}{s}\nabla \cdot (\eta(\vec{r})\nabla\varphi(\vec{r})), \tag{6}$$

with the boundary conditions $\varphi(x, y, z = 0) = 0$, and $\varphi(x, y, z = L) = L$ (i.e., average $E_z = -1$), the potential φ may be formally solved as

$$\varphi = z + \frac{1}{s}\hat{\Gamma}\varphi, \tag{7a}$$

or

$$\varphi - \frac{1}{s}\hat{\Gamma}\varphi = z. \tag{7b}$$

Eq. (7b) has a formal solution, given by

$$\varphi = \left(1 - \frac{1}{s}\hat{\Gamma}\right)^{-1} z. \tag{7c}$$

Here $\hat{\Gamma}$ is an integral operator defined by

$$\hat{\Gamma} = \int \mathrm{d}V'\eta(\vec{r}')\nabla' G(\vec{r}, \vec{r}') \cdot \nabla', \tag{8}$$

and $G(\vec{r}, \vec{r}') = 1/4\pi|\vec{r} - \vec{r}'|$ is the Green function of the Laplacian. The integral operator $\hat{\Gamma}$ is a projection operator as can be seen from Eq. (8), since the Green function may be regarded as the inverse of the Laplacian operator (two successive gradient operators). Hence the eigenvalues of $\hat{\Gamma}$ lie between 0 and 1. The integral operator $\hat{\Gamma}$ is Hermitian under the following definition of the inner product:

$$\langle\psi|\varphi\rangle = \int \mathrm{d}V\eta(\vec{r})\nabla\psi^*(\vec{r}) \cdot \nabla\varphi(\vec{r}). \tag{9}$$

If φ_u and s_u are respectively the eigenfunctions and their associated eigenvalues of the integral (Hermitian) operator $\hat{\Gamma}$, then it is possible to express the *zz* component of the effective dielectric tensor, $\bar{\varepsilon}_{zz}$, as the volume-averaged value of D_z divided by the volume averaged value of the electric field, given simply by $E_z = -1$. That is,

$$\begin{aligned}\bar{\varepsilon}_{zz} &= \frac{1}{V}\int \mathrm{d}V[\varepsilon_\ell(1 - \eta(\vec{r})) + \varepsilon_s\eta(\vec{r})]\frac{\partial\varphi(\vec{r})}{\partial z} \\ &= \varepsilon_\ell\left(1 - \frac{1}{V}\int \mathrm{d}V\frac{1}{s}\eta(\vec{r})\nabla\varphi \cdot \nabla z\right) \\ &= \varepsilon_\ell\left(1 - \frac{s^{-1}}{V}\langle z|\varphi\rangle\right).\end{aligned} \tag{10}$$

By substituting Eq. (7c) for $|\varphi\rangle$ in Eq. (10), we obtain

$$\begin{aligned}\bar{\varepsilon}_{zz} &= \varepsilon_\ell\left(1 - \frac{1}{V}\langle z|\left(s - \hat{\Gamma}\right)^{-1}|z\rangle\right) \\ &= \varepsilon_\ell\left(1 - \frac{1}{V}\sum_u\langle z|\left(s - \hat{\Gamma}\right)^{-1}|\varphi_u\rangle\langle\varphi_u|z\rangle\right),\end{aligned}$$

where we have denoted the eigenfunctions of the $\hat{\Gamma}$ operator as φ_u (with associated eigenvalue s_u), defined as $\hat{\Gamma}\varphi_u = s_u\varphi_u$, with $\sum_u |\varphi_u\rangle\langle\varphi_u| = 1$, the identity matrix. From the above we obtain the *spectral representation* of $\bar{\varepsilon}_{zz}$ as

$$\bar{\varepsilon}_{zz} = \varepsilon_\ell \left(1 - \frac{1}{V}\sum_u \frac{|\langle z|\varphi_u\rangle|^2}{s - s_u}\right). \tag{11}$$

Here V is the sample volume, a normalization factor. The most remarkable feature of Eq. (11), which is exact, is the fact that material properties, given by s, are *completely separated from the geometric information* (contained in φ_u and s_u) as "filtered" by the Laplacian. Since both the solid and liquid dielectric constants can be complex, s is a complex number in general. At the same time, it is clear that if s is real, then its value as given by Eq. (5b) should be either less than zero or greater than 1, as noted before. Since both $|\langle z|\varphi_u\rangle|^2$ and s_u are real, with the additional constraint that $0 < s_u < 1$ as already stated, it follows that $s - s_u$ can approach zero only in limiting cases, and these cases define the upper bounds for the shear modulus and yield stress, described below.

Eq. (11) makes clear that the imaginary parts of the dielectric constants can indeed contribute to $\mathrm{Re}(\bar{\varepsilon}_{zz})$ (through the complex material parameter s), and hence the ER effect.

2.3. Computational formalism

We would like to use the spectral representation to accurately evaluate the effective dielectric constant for different periodic structures formed by micro/nanospheres, and identify the ground state structure which should have the largest $\mathrm{Re}(\bar{\varepsilon}_{zz})$ in accordance with the variational principle stated earlier. Here the assumption is that the ground state structure is unique and therefore must be periodic. However, as seen from Fig. 2 the ER microstructure consists of two scales. On the macroscale there is a clear phase separation when a strong electric field is applied so that $\gamma \gg 1$. The two phases in the ER fluid are the dense "column" phase and the fluid phase, and the overall effective dielectric constant must be a suitable average of the two. If we denote the dielectric constant of the columns as $\bar{\varepsilon}^{zz}_{col}$, the volume fraction of spheres inside the column as p_{col}, and the overall volume fraction of solid spheres as p, then it is well-known that for the column geometry, the overall effective dielectric constant is simply the arithmetic average:

$$\bar{\varepsilon}_{zz} = \frac{p}{p_{col}}\bar{\varepsilon}^{zz}_{col} + \left(1 - \frac{p}{p_{col}}\right)\varepsilon_\ell. \tag{12}$$

The spectral function approach can be used to accurately predict $\bar{\varepsilon}^{zz}_{col}$ for different microscale periodic structures inside the column. Since the column is finite in cross-section, its surface energy can also be evaluated. It has been found that the surface energy is $\sim 10^{-3}$ times smaller than that of the bulk [19]. Hence for all practical purposes we can ignore the small surface energy and treat the column as infinite crystals in our evaluation of $\bar{\varepsilon}^{zz}_{col}$.

It should be noted that the accurate calculation of $\bar{\varepsilon}^{zz}_{col}$ is usually outside the capability of most effective medium theories, since these theories are generally suitable for random media and hence can not distinguish between the different periodic structures.

To obtain $\bar{\varepsilon}^{zz}_{col}$ numerically, Eq. (7b) may be solved by expanding the potential φ in terms of complete, orthogonal basis functions [19], so that Eq. (7b) is expressed as a set of linear simultaneous equations with the expansion coefficients as the unknowns. In particular, if we use local basis functions (spherical basis, see below) to expand the potential inside each solid sphere, then Eq. (7b) may be written as

$$\sum_{\vec{R}'}\sum_{\ell',m'}\left(\delta_{\vec{R}\vec{R}'}\delta_{\ell\ell'}\delta_{mm'} - \frac{1}{s}\hat{\Gamma}_{\ell m,\ell' m'}(\vec{R}-\vec{R}')\right)A_{\ell' m'}(\vec{R}') = z_{\ell m}(\vec{R}), \tag{13}$$

where $A_{\ell m}(\vec{R})$ denotes the expansion coefficient of the potential inside a sphere centered at $\vec{R}$, the subscript indices ℓ, m denote the spherical harmonics,

$$\hat{\Gamma}_{\ell' m',\ell m}(\vec{R}-\vec{R}') = \langle\chi_{\ell' m'}(\vec{r}-\vec{R}')|\hat{\Gamma}|\chi_{\ell m}(\vec{r}-\vec{R})\rangle \tag{14}$$

denotes the matrix element of the operator $\hat{\Gamma}$, and $z_{\ell m}(\vec{R}) = \langle\chi_{\ell m}(\vec{r}-\vec{R})|z\rangle$. Here $\chi_{\ell m}(\vec{r}-\vec{R}) = f_\ell(|\vec{r}-\vec{R}|)Y_{\ell m}(\theta,\phi)$ denotes the local spherical basis function centered at $\vec{R}$. The periodic structure enters through the matrix elements as expressed by Eq. (14), where $\vec{R}$ denotes the lattice vectors.

In order to choose the local basis function so that the matrix elements and the right-hand side may be explicitly evaluated, we would like to have $\chi_{\ell m}$'s be the eigenfunctions of the $\hat{\Gamma}$ operator for a single sphere with radius a. That is, we would like to have

$$\begin{aligned}\hat{\Gamma}\chi_{\ell m}(\vec{r}) &\equiv \int d\vec{r}'\eta(\vec{r}')\nabla' G(\vec{r},\vec{r}')\cdot\nabla'\chi_{\ell m}(\vec{r}') \\ &= \int dS'\hat{n}\cdot\nabla' G(\vec{r},\vec{r}')\chi_{\ell m}(\vec{r}') + \chi_{\ell m}(\vec{r})\eta(\vec{r}) \\ &= s_{\ell m}\chi_{\ell m}(\vec{r}).\end{aligned} \tag{15a}$$

Here we have let $\vec{R} = 0$, $\eta(\vec{r}) = 1$ for $|\vec{r}| < a$, and zero otherwise; $\hat{n}$ denotes the outward normal at the surface of the sphere, and $s_{\ell m}$ denotes the eigenvalue of the local eigenvector/basis function. In Eq. (15a), integration by parts has been performed in going from the first line to the second line.

By using the spherical harmonics expansion for the Green function,

$$G(\vec{r},\vec{r}') = \frac{1}{4\pi|\vec{r}-\vec{r}'|} = \sum_{\ell m}\frac{1}{2\ell+1}\frac{r_<^\ell}{r_>^{\ell+1}}Y_{\ell m}(\theta,\phi)Y^*_{\ell m}(\theta',\phi'),$$

with $r_< = \min(r, r')$ and $r_> = \max(r, r')$, Eq. (15a) can be re-written as

$$a^2\frac{\ell}{2\ell+1}\frac{a^{\ell-1}}{r^{\ell+1}}f_\ell(a) = s_{\ell m}f_\ell(r), \quad r > a, \tag{15b}$$

$$-a^2\frac{\ell+1}{2\ell+1}\frac{r^\ell}{a^{\ell+2}}f_\ell(a) + f_\ell(r) = s_{\ell m}f_\ell(r), \quad r < a. \tag{15c}$$

Eqs. (15b) and (15c) can be easily solved explicitly, leading to

$$f_\ell(r) = \left(\frac{r}{a}\right)^\ell\frac{1}{\sqrt{a\ell}} \quad \text{for } r < a, \tag{16a}$$

$$f_\ell(r) = \left(\frac{a}{r}\right)^{\ell+1}\frac{1}{\sqrt{a\ell}} \quad \text{for } r \geq a, \tag{16b}$$

with $s_{\ell m} = \ell/(2\ell+1)$. Here $\ell = 1, 2, 3, \ldots$, and $-\ell \leq m \leq \ell$. With this basis function, one can obtain

$$\begin{aligned}\langle\chi_{\ell m}|z\rangle = z_{\ell m} &= \int d\vec{r}\eta(\vec{r})\nabla z\cdot\nabla\chi_{\ell m} = \hat{e}_z\cdot\int d\vec{r}\eta(\vec{r})\nabla\chi_{\ell m} \\ &= -\hat{e}_z\cdot\int d\vec{r}\chi_{\ell m}\nabla\eta(\vec{r}) = \int d\vec{r}(\hat{e}_z\cdot\hat{r})\delta(r-a)\chi_{\ell m} \\ &= \int d\Omega a^2\cos\theta Y_{\ell m}(\theta,\phi)\frac{1}{\sqrt{a\ell}} \\ &= \left(\frac{4\pi a^3}{3}\right)^{1/2}\delta_{\ell 1}\delta_{m0},\end{aligned} \tag{17}$$

which is noted to be independent of $\vec{R}$. In the above we have used the fact that $\nabla\eta(\vec{r}) = -\delta(r-a)\hat{r}$, where $\hat{r}$ means a unit vector along the outward radial direction. The matrix elements can also be similarly obtained as

$$\begin{aligned}\hat{\Gamma}_{\ell'm',\ell m}(0-\vec{R}) &= \langle \chi_{\ell'm'}(\vec{r}-\vec{R})|\hat{\Gamma}|\chi_{\ell m}(\vec{r})\rangle \\ &= s_{\ell m}\langle \chi_{\ell'm'}(\vec{r}-\vec{R})|\chi_{\ell m}(\vec{r})\rangle \\ &= s_{\ell m}\int \mathrm{d}\vec{r}\,\eta(\vec{r})\nabla\chi_{\ell'm'}(\vec{r}-\vec{R})\cdot\nabla\chi^*_{\ell m}(\vec{r}) \\ &= s_{\ell m}a^2\int \mathrm{d}\Omega\,\chi_{\ell'm'}(\vec{a}-\vec{R})\hat{r}\cdot\nabla\chi^*_{\ell m}(\vec{a}), \end{aligned} \tag{18}$$

where integration by parts has been performed in going from the third to the fourth line, using again $\nabla\eta(\vec{r}) = -\delta(r-a)\hat{r}$. The matrix elements may be explicitly evaluated with the aid of the following formula:

$$\begin{aligned}&\frac{1}{|\vec{r}-\vec{R}|^{\ell'+1}}\int Y^*_{\ell m}(\Omega_{\vec{r}})Y_{\ell'm'}(\Omega_{\vec{r}-\vec{R}})\mathrm{d}\Omega_{\vec{r}} \\ &\quad= (-1)^{\ell'+m'}\left[\frac{(2\ell+1)(2\ell'+1)}{(\ell+m)!(\ell-m)!(\ell'+m')!(\ell'-m')!}\right]^{1/2} \\ &\qquad\times\frac{r^\ell}{R^{\ell+\ell'+1}}\frac{(\ell+\ell'+m-m')!}{2\ell+1} \\ &\qquad\times P^{m'-m}_{\ell+\ell'}(\theta_{\vec{R}})\exp[\mathrm{i}(m'-m)\phi_{\vec{R}}]. \end{aligned} \tag{19}$$

Some explicit expressions for the matrix elements can be found in Ref. [19].

We return to Eq. (13) and note that as the right-hand side is independent of $\vec{R}$, we can Fourier-transform the whole equation to the wavevector domain as

$$\sum_{\ell',m'}\left(\delta_{\ell\ell'}\delta_{mm'}-\frac{1}{s}\hat{\Gamma}_{\ell m,\ell'm'}(\vec{K})\right)A_{\ell'm'}(\vec{K}) = z_{\ell m}\delta_{\vec{K},0}. \tag{20}$$

Here the $\vec{K}$ vectors are the reciprocal wavevectors in the first Brillouin zone of the periodic structure. In the form of Eq. (20), it is clear that only the $\vec{K}=0$ component has a nontrivial solution. That is, with the right hand side being non-zero only for $\vec{K}=0$, all $A_{\ell m}(\vec{K})=0$ for $\vec{K}\neq 0$, because the determinant of the matrix on the left hand side of Eq. (20) is always non-zero, as the eigenvalues of the $\hat{\Gamma}$ operator are always between 0 and 1, whereas the value of s as defined by Eq. (5b) can not be in that interval. It follows that we only need to solve the following equation for the *homogenized* ($\vec{K}=0$) operator:

$$\sum_{\ell',m'}\left(\delta_{\ell\ell'}\delta_{mm'}-\frac{1}{s}\hat{\Gamma}^{(0)}_{\ell m,\ell'm'}\right)A_{\ell'm'} = z_{\ell m}, \tag{21a}$$

where

$$\hat{\Gamma}^{(0)}_{\ell m,\ell'm'} = \sum_{\vec{R}}\hat{\Gamma}_{\ell m,\ell'm'}(\vec{R}), \tag{21b}$$

i.e., a summation of the matrix elements over all the lattice vectors. However, for the purpose of evaluating the effective $\bar{\varepsilon}_{zz}$, it is not necessary to solve Eq. (21a). Instead, we can directly obtain $\bar{\varepsilon}_{zz}$ from the eigenvalues and eigenfunctions of the $\hat{\Gamma}^{(0)}_{\ell m,\ell'm'}$ matrix. That is, if we express the (global) eigenfunction of the $\hat{\Gamma}^{(0)}$ operator as $\varphi^{(0)}_u = \sum_u \varphi^{(u)}_{\ell m}\chi_{\ell m}$ with the eigenvalue s_u, then

$$\sum_{\ell',m'}\left(\delta_{\ell\ell'}\delta_{mm'}-\frac{1}{s_u}\hat{\Gamma}^{(0)}_{\ell m,\ell'm'}\right)\varphi^{(u)}_{\ell m} = 0. \tag{22}$$

From Eq. (11) we have

$$\begin{aligned}\bar{\varepsilon}^{zz}_{col} &= \varepsilon_\ell\left(1-\frac{1}{V}\sum_u\frac{|\langle z|\varphi_u\rangle|^2}{s-s_u}\right) \\ &= \varepsilon_\ell\left(1-\frac{1}{V}\sum_{\vec{R},\ell,m}\sum_u\frac{|\langle z|\chi_{\ell m}\rangle\langle\chi_{\ell m}|\varphi^{(0)}_u\rangle|^2}{s-s_u}\right) \\ &= \varepsilon_\ell\left(1-\frac{N}{V}\sum_u\sum_{\ell m}\frac{|z_{\ell m}\varphi^{(u)}_{\ell m}|^2}{s-s_u}\right) \\ &= \varepsilon_\ell\left(1-p_{col}\sum_u\frac{|\varphi^{(u)}_{10}|^2}{s-s_u}\right) \end{aligned} \tag{23}$$

where the summation over $\vec{R}$ is noted to give a factor of N, since both $z_{\ell m}$ and $\varphi^{(u)}_{\ell m}$ are *independent of* $\vec{R}$. The resulting V/N yields the unit cell volume. By recalling the result of Eq. (17) for $z_{\ell m}$, we arrive at the final answer shown above.

Two technical points should be noted. First, the summation over the lattice vectors in Eq. (21b) should be carried out by using the Ewald summation method, since otherwise the convergence can be a problem. Second, there has to be a slight separation between the microspheres, in order to avoid the summation over very large values of angular momentum index ℓ that would be needed otherwise.

In what follows, we shall also treat the cases of *singly or doubly coated microspheres*, which need only slightly modified computational formalisms. For example, instead of the $f_\ell(r)$ (of the basis function) as given by Eqs. (16a) and (16b), the radial component of the basis function would be slightly more complicated in the coated cases. In addition to the summations over (ℓ, m), there is also the coating layer index which needs to be added. These details will be treated as self evident and therefore not further detailed here.

3. Predictions and comparison with experiments

By using the spectral representation and the effective dielectric constant formulation, quantitative predictions become possible for the microstructure, shear modulus, yield stress, and other related characteristics associated with an ER fluid comprising uniform-sized microspheres dispersed in an insulating liquid. In particular, upper bounds can be derived for the shear modulus and the yield stress.

3.1. *Ground state microstructure*

For uniform-sized microspheres, the lowest energy state should correspond with a periodic microstructure which maximizes the overall (real part of the) *zz* component of the effective dielectric constant. By calculating the effective dielectric constants for the six structures of body centered tetragonal (BCT), face centered cubic (FCC), hexagonal close-packed (HCP), body centered cubic (BCC), simple cubic (SC), and diamond, it was found that at any fixed concentration of solid microspheres, the magnitude of the effective dielectric constant always arranges themselves in the above decreasing order, with FCC and HCP a very close second to the BCT [7,13,19]. The calculated values of $\bar{\varepsilon}_{zz}$ for the various structures are shown in Table 1, at two ratios of $\varepsilon_s/\varepsilon_\ell = 10$ and 800. For comparison, results using just the dipole approximation are also shown.

In Table 1, it should be noted that the values of the effective dielectric constants given are those averaged over the whole sample, as given by Eq. (12). That is, for the effective dielectric constant values inside the close-packed columns, the FCC value is in fact slightly larger than that for the BCT, owing to the higher packing density (higher p_{col}). However, when averaged over the whole sample in accordance with Eq. (12), the BCT wins slightly, mainly because of BCT's lower p_{col} (than the FCC) and hence a larger value for p/p_{col} (and thereby giving more weight to its $\bar{\varepsilon}^{zz}_{col}$). It turns out that BCT always wins slightly, regardless of the values of the material constants and solid volume fractions.

Table 1
The exact effective dielectric constants of several periodic structures, compared with that in the dipolar approximation. The separation between the spheres is 5×10^{-3} in terms of the sphere radius, volume fraction of particles is 0.2.

$\varepsilon_s/\varepsilon_\ell$		Structure					
		BCT	FCC	HCP	BCC	SC	Diamond
10	Exact	2.167	2.156	2.156	2.043	1.911	1.627
	Dipole	2.031	1.994	1.995	1.905	1.734	1.601
800	Exact	5.173	5.129	5.129	4.205	3.518	1.976
	Dipole	3.376	3.188	3.194	2.798	2.230	1.897

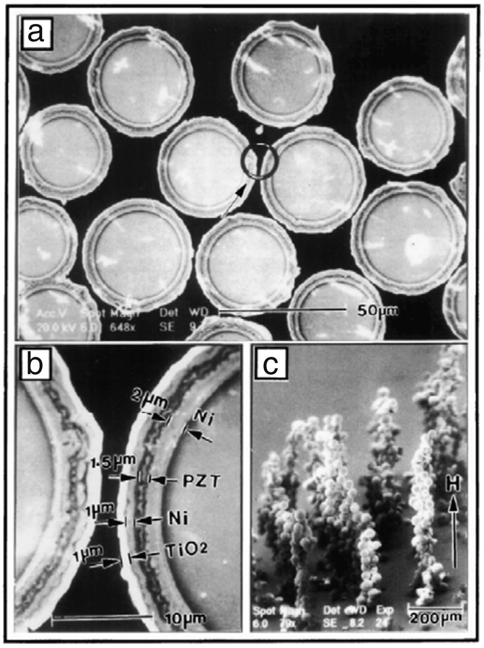

Fig. 3. (a) Cross-sectional SEM picture of the coated spheres. The apparent size variation is caused by a deviation of the spheres' centers from the cutting plane. The arrow points to a circular region detailed in (b), which shows a detailed thickness of the four coatings. From the inside out: 2 μm Ni, 1.5 μm PZT, 1 μm Ni, and finally 1 μm TiO_2. (c) The coated EMR spheres under the influence of a small magnetic stirrer.

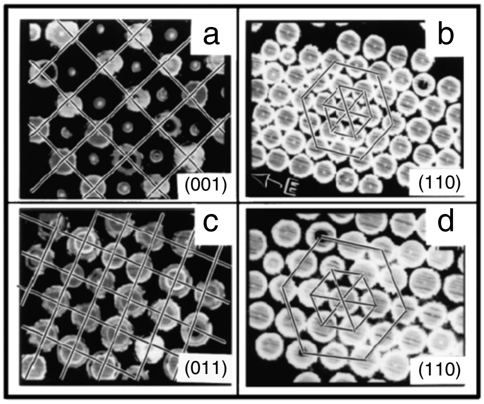

Fig. 4. (a)–(b) BCT structure formed by multiply-coated microspheres under an electric field (2 kV/mm). The structure is frozen in epoxy and visualized through cross-sectional SEM micrographs. (c)–(d) are the signatures of a FCC structure formed by the same multiply-coated microspheres under crossed electric field (2 kV/mm) and magnetic field (54 G).

3.2. Structural transition under crossed electric and magnetic fields

BCT is the ground state microstructure for the microspheres inside the solid columns formed under an external electric field. This prediction remains unchanged for any ratio of the solid and liquid dielectric constants, and also remains true if the electrostatic interaction between the solid microspheres is treated only within the dipole approximation.

An interesting phenomenon occurs if the microspheres are not only responsive to the electric field but also to the magnetic field (e.g., by using Ni coating so that each microsphere can have a small permanent magnetic moment), then under crossed electric and magnetic fields there can be a structural Martensitic transition in the ground state structure, from BCT to FCC [15]. Physically this is based on the minimization of the electrostatic energy plus the magnetic energy, both treated in a similar fashion. As the magnetic field increases and its energy becomes comparable to that of the electric energy, the ground state structure inevitably would tend towards a more symmetric structure along the two directions of the electric and magnetic fields, hence the FCC structure.

3.3. Experimental verification of the ground state structure predictions

Experimentally [15], microspheres with a glassy core of 34 ± 2 μm were multiply coated by a 2 μm layer of Ni, a 1.5 μm layer of lead zirconate titanate (PZT), another 1 μm layer of Ni, and finally 1 μm layer of TiO_2. The overall diameter of the microspheres is thus 45 ± 2 μm. A cross-sectional SEM picture of the coated spheres is shown in Fig. 3(a). The apparent size variation is caused by a deviation of the spheres' centers from the cutting plane. A more detailed picture of the coatings is shown in Fig. 3(b). The magnetic response of these multiply-coated microspheres is demonstrated in Fig. 3(c), in which the microspheres are shown to stagger upright under the influence of a small magnetic stirrer. We first investigate the ground state microstructure under an electric field of $E = 2\ \mathrm{kV\,mm^{-1}}$ when the microspheres were dispersed in epoxy. After solidifying the epoxy matrix, the sample was cut along the (001) and (110) planes and visualized with SEM images. They are shown in Fig. 4(a) and (b) as clear-cut evidences for the BCT structure.

A separate sample with similar composition was subsequently prepared and subjected to the same electric field but a varying magnetic field. The structural transition was monitored by measuring the small dielectric constant variation in the direction perpendicular to both the electric and magnetic fields. A clear minimum in the dielectric constant was observed in every case, between 50 G and 80 G. When the magnetic field is larger than that, the dielectric constant returns to that observed at the low field limit, indicating that the BCT structure is now established along the magnetic field direction instead of the electric field direction. However, in the interesting region of the minimum, we had obtained many cross-sectional micrographs by freezing in solid epoxy the configurations at various magnetic field values, and cutting the resulting samples [15]. The results are shown in Fig. 4(c) and (d). They indicate a square lattice in the (011) plane (the FCC {100}) and a hexagonal lattice in the (110) (the FCC {111}), both the signatures of a FCC structure.

The direct observation of the ground state microstructure and its Martensitic transition under crossed electric and magnetic fields clearly demonstrates the appearance of self-organized microstructures under external field(s), as predicted from energy considerations. They also confirm the structural predictions of the variational approach.

3.4. Shear modulus and yield stress

From the known ground state microstructure, one can calculate the shear modulus and yield stress by first defining the shear distortion. This is shown in the inset to Fig. 5. Here θ, the angle of distortion relative to the external E field, is the strain variable.

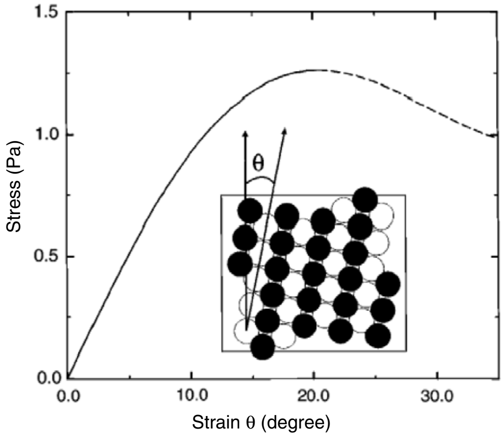

Fig. 5. Calculated stress, in units of Pascal, plotted as a function of strain, i.e., the tilt angle θ as defined in the inset. The dashed line indicates the unstable regime. The maximum stress is defined as the static yield stress. Here the curve is calculated with $\varepsilon_\lambda = 2.7$, $\varepsilon_s = 8.4 + 0.43\mathrm{i}$, the volume fraction of spheres is 22%, and the applied field is 1.3 kV/mm.

For the BCT lattice, shearing in the direction perpendicular to the z axis means not only a tilt away from the electric field direction by an angle θ, but also a distortion in the lattice constants c and a given by $c/R = 2/\cos\theta$, $a/R = [8 - (c^2/2R^2)]^{1/2}$. Consequently, under shear the volume fraction of solid spheres in the BCT structure is also θ dependent. For a small θ, $\bar{\varepsilon}_{zz}(\theta)$ may be expanded about its optimal value as

$$\mathrm{Re}\left[\frac{\bar{\varepsilon}_{zz}(\theta)}{\varepsilon_\ell}\right] = \mathrm{Re}\left[\frac{\bar{\varepsilon}_{zz}(0)}{\varepsilon_\ell}\right] - \frac{1}{2}\mu\theta^2 + \cdots, \tag{24}$$

where μ denotes the shear modulus. For finite distortions, the effective dielectric constant can again be calculated using the spectral representation, leading to an energy as a function of, $E(\theta)$. By definition the stress is given by $\mathrm{d}E(\theta)/\mathrm{d}\theta$. A numerically evaluated stress versus strain curve [13] is shown in Fig. 5. It is seen that at a small strain, the stress varies linearly with strain. The slope of the linear variation is precisely the shear modulus. Also, the peak of the stress–strain curve corresponds to the yield stress (at the position of maximum strain) beyond which the system becomes unstable.

What happens beyond the peak of the stress–strain curve is in the domain of ER fluid dynamics, to be treated in Section 6.

3.5. Experimental verification of yield stress predictions

To experimentally verify the yield stress prediction, we utilize the relaxational effect of the dielectric constant that would generally appear at finite frequencies (of the applied electric field) [13,16]. It has been widely known in the field of ER fluid research that any presence of water in the sample can enhance the ER effect, sometimes dramatically. Water is also known to have a relaxational dielectric constant that can be strongly frequency dependent. In addition, water has a fairly large real part of the dielectric constant, and it was suspected that the early detected ER effect was due to the presence of water. However, water can disappear starting at temperatures > 60 °C, and hence can cause unreliable performance. The ER fluids produced after the 1980's have been especially noted to avoid any presence of water, e.g., in our experiments on visualizing the ground state microstructures, all samples were heated to 120 °C for 24 h prior to measurements. However, the role of water has always been intriguing, and a systematic study of the role of water would not only be informative in relation to the theory predictions, but also may be enlightening in the search for a type of colloids with an enhanced ER effect.

Three samples were prepared, consisting of 1.5 μm diameter microspheres dispersed in silicone oil. The samples were first baked to remove any trace of water, and then measured amounts of 5 vol.% (denoted sample 1), 8 vol.% (sample 2), and 11.4 vol.% (sample 3) water were introduced. With a cell consisting of two parallel plate electrodes, the dielectric measurements of the ER fluids were performed by an HP4284A LCR meter in a frequency range of 20 Hz to 100 kHz. The static yield stress was measured by using a standard parallel plate torsional device with a root-mean-square (RMS) electric field of 510 V/mm applied across the ER fluids sandwiched between the two parallel plates. The lower plate was rotated slowly, dragging the top plate with a torque, which was connected via a torque meter to the top plate. The static yield stress was read out when slipping occurred between the two plates, after subtracting off the zero-field value (which is about 1% of the high-field value). The static yield stress was observed to have an accurate E^2 field strength dependence. The real and imaginary parts of the effective dielectric constants of the three samples were measured as a function of frequency [16], shown as symbols in Fig. 6. These data were used to determine the (frequency dependent) effective dielectric constants of the solid particles and the fluid, by assuming the water to *coat* the glass microspheres, with the excess water dispersed in silicone oil. Excellent fittings can be obtained, shown as the solid lines in Fig. 6.

With the material parameters thus determined, we compare the measured and predicted yield stress of the three samples in Fig. 7, again as a function of the applied electric field frequency. A reasonably good agreement is seen. Thus yield stress can be quantitatively predicted, provided the correct material parameters and geometric information are supplied.

Besides verifying the yield stress predictions, this study also shows that even a small amount of water can have a dramatic effect. This is possible only if the water coats the solid particles, or inserts itself in the region of two touching microspheres. The thought that led to the discovery of the giant electrorheological effect, described below, is that if the OH group can somehow be fixed on the solid microspheres, then the dramatic effect seen here may be usefully utilized to enhance the ER effect, with no adverse consequences.

3.6. Upper bounds

A particularly important result from the effective dielectric constant formulation is the upper bounds to the shear modulus and yield stress. This result can in fact be intuitively appreciated from Eq. (11). Since both the shear modulus and yield stress are related to the real part of the effective dielectric constant, the upper bounds to these quantities will be determined by the divergence of $\bar{\varepsilon}_{zz}$. From Eq. (11) this can only happen when the denominator on the right hand side vanishes. From the definition of s and the fact that s_u is always real and between 0 and 1, the divergence of $\bar{\varepsilon}_{zz}$ would happen when both s and s_u approach either 0 or 1. Here we present only the case of the 0 limit. To obtain the physical upper bounds, we let $\varepsilon_s \to \infty$ so that $s \to 0$. We also note that s_u would approach zero only when the spheres touch. Hence we specify a (small) separation, δ, between the surfaces of the neighboring spheres, and evaluate the shear modulus and yield stress as a function of the ratio δ/R, where R is the sphere radius. The upper bounds thus obtained are $1.9\,(R/\delta)$ for the shear modulus, and $1.38\sqrt{R/\delta}$ for the static yield stress, both in units of the energy density $\varepsilon_\ell E^2/8\pi$. For $\delta = 1$ Å (atomic separation) and $R = 20$ μm, we get $15{,}120(\varepsilon_\ell E^2)$ for the maximum shear modulus and $24.6(\varepsilon_\ell E^2)$ for the maximum yield stress. If $\varepsilon_\ell = 2.5$ and $E = 1\ \mathrm{kV\ mm^{-1}}$, these expressions translate into 5 MPa and 8 kPa, respectively. It should be noted that both upper bounds increase monotonically with the size of the microspheres, and that the unit

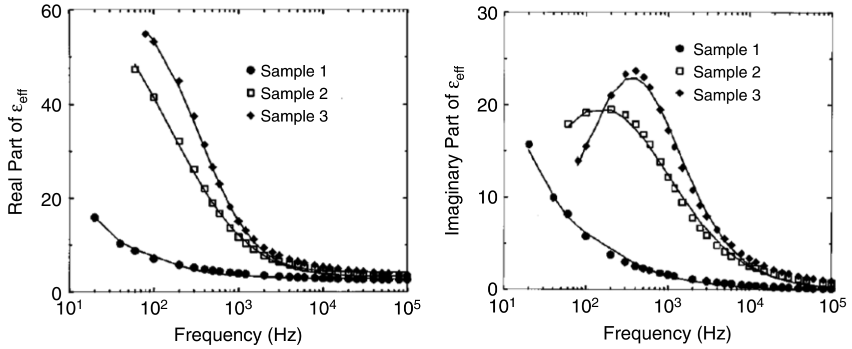

Fig. 6. The real and imaginary parts of effective dielectric constants for the three samples plotted as a function of frequency. The symbols represent the experimental measurements and lines are fitted theoretical calculations. The free material parameters of the model [16] are determined by the fittings.

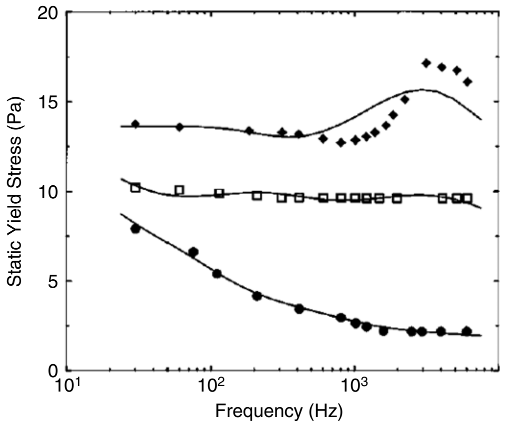

Fig. 7. The measured (symbols) and calculated (lines) static yield stress plotted as a function of frequency. From bottom to top: sample 1, sample 2, and sample 3, in the order of an increasing amount of water.

is quadratic in the electric field. Both are the consequences of the induced polarization mechanism. In particular, as the electrostatic energy density in a polarizable medium is generally given by $-\vec{P}\cdot\vec{E}$, where $\vec{P}$ is the dielectric polarization, then $\vec{P} \propto \vec{E}$ directly yields the quadratic dependence. The $\sqrt{R}$ dependence for the upper bound of the static yield stress may be understood heuristically as follows from the capacitance between two spheres, which diverges as $\ell n(R/\delta)$.

Under an applied electric field $\vec{E}$ along the axis joining the centres of the two spheres, the leading order term of the free energy density is proportional to the capacitance. If now we apply a shear perpendicular to the electric field, the line segment joining the centers of the two spheres will both be tilted at an angle θ with respect to the electric field direction, as well as lengthened. If the new separation is denoted by d, then $(2R + d)\cos\theta = 2R + \delta$, so that $d \approx \delta + R\theta^2$ for a small θ. Within the small angle approximation, the shear stress is proportional to $-(\partial C/\partial\theta) \propto (R/d)[(d-\delta)/R]^{1/2}$, which is noted to have a peak value given by the condition $d = 2\delta$, so that the static yield stress $\propto (R/\delta)^{1/2}$.

3.7. *Experimental verification of the upper bound prediction*

To verify the particle size R and δ dependencies of the yield stress upper bound, doubly-coated microspheres were fabricated with uniform-sized glassy core and nickel and titania (TiO_2) outer coatings, using sequentially the electroless plating (for the nickel coating) and sol–gel (for the titania coating) methods. Two different sizes of the core glass microspheres, 1.5 μm and 50 μm in diameter, were used. A cross-sectional picture of the multiply-coated spheres is shown in Fig. 8(a–c). Here the nickel coating serves the purpose of making the microspheres polarizable enough so that we can take s to be nearly zero, and the silica coating serves the purpose of setting a value for δ. In Fig. 9(a,b) we compare the measured yield stress values (symbols) with those calculated from the effective dielectric constant formulation. The increased size of the particles is clearly seen to increase the yield stress, in approximately the square-root ratio as predicted by the upper bound expression. In addition, the absolute values of the measured yield stress are also well-accounted for by the calculations using approximate values of the titania coating thicknesses. For comparison, we have also measured and calculated the yield stresses for pure glass spheres, and those with just titania coatings. Both are orders of magnitude smaller (as seen by the lines lying close to the horizontal axis). The dashed line is the calculated value for pure titania spheres of similar size. It is also much smaller. The simple physical picture that emerges from these results is that (1) ER yield stress is closely related to the electrostatic energy of the system, and (2) for a given applied electric field, the electrostatic energy can be maximized by field distribution and dielectric

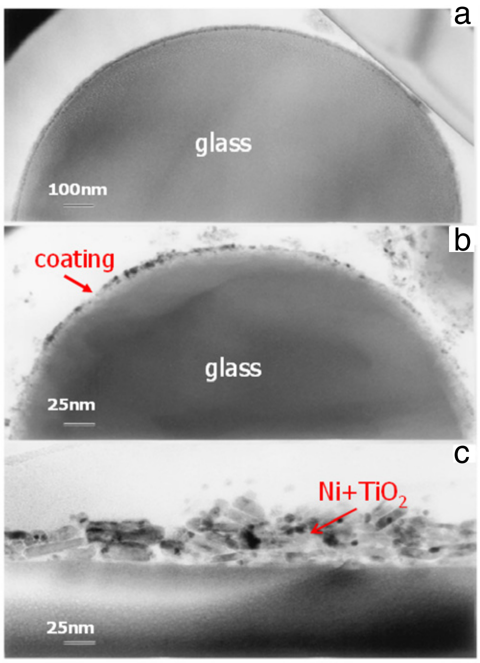

Fig. 8. Cross sectional electron micrographs for (a) 1.5 μm nickel coated, (b) 1.5 μm doubly coated, and (c) 50 μm doubly coated particles. The scale bar is 100 nm and 25 nm for (a), (b), and (c), respectively. While in (a), the metal/glass interface is clearly visible, diffusion of Ni atoms, probably from the heating process, blurred this boundary, as shown in (b) and (c). TheTiO_2 coating thickness is seen to be in the range of 10 to 30 nm for (b) and 25 to 60 nm for (c).

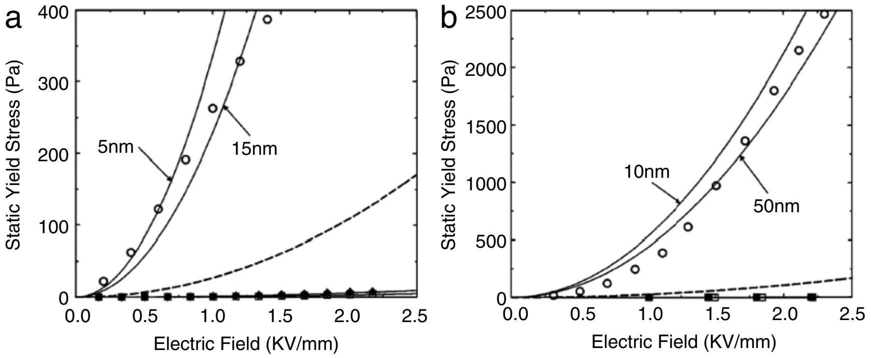

Fig. 9. The measured (symbols) and calculated (lines) static yield stress of ER fluid using (a) 1.5 μm doubly coated particles, (b) 50 μm doubly coated particles. From the vertical scales it is seen that the larger particles exhibit a larger yield stress in roughly the square-root of the size ratio. For comparison, we have also shown the calculated yield stress for solid TiO_2 particles of the same sizes (dashed lines), as well as the measured yield stress for pure glass spheres (almost invisible as the open squares on the horizontal axis) of the same size, as well as the measured yield stress for glass spheres coated just by TiO_2, without the Ni (black diamonds on the horizontal axis) of the same size.

constant of the materials. The metallic coating of the doubly-coated microspheres limits the field to the dielectric areas occupied by the titania coating and the silicone oil. The thin titania coatings ensure small separations, thus producing high internal fields. The enhanced ER effect is the result.

The doubly coated glassy microspheres are in a sense "ideal" for the ER effect. However, the requirement of large sphere size is not optimal from the applications point of view, since large microspheres also tend to sediment, unless the density can be matched with that of the fluid.

3.8. Anisotropy and nonlinearity of the effective dielectric constant

Since the theoretical approach is based on the effective dielectric constant optimization, it is important to check experimentally if the dielectric constant indeed increases and displays anisotropy under the application of an electric field. However, measurement-wise it is difficult to determine the dielectric constant along the electric field direction, especially when the applied field is fairly large. In order to overcome this difficulty, we have utilized the similarity in the microstructure under an electric field with that under a magnetic field. For this experiment, special particles were prepared whereby silica spheres 35 ± 3 μm in diameter were coated with an inner Ni layer and an outer dielectric layer, such as lead zirconate titanate (PZT) or TiO_2, formed by using electroless plating and sol gel processes, respectively. The microstructures formed by applying a magnetic field are shown in Fig. 10. The dielectric constants along the z (magnetic field direction) and x directions ($\bar{\varepsilon}_{zz}$ and $\bar{\varepsilon}_{xx}$), measured by an LRC meter, are shown in Fig. 10 [19]. It is seen that whereas the zz component of the effective dielectric constant displays an increasing trend with the magnetic field, just as expected, the xx component displays a slight decrease. These trends are independent of whether the outer coating is PZT or TiO_2. The theoretical predictions of the asymptotic dielectric constant values, again obtained by using the spectral function approach, are shown in Table 2. Here the inputs to the calculations are determined by the values of the real and imaginary parts of the effective dielectric constants when the system is isotropic ($H = 0$). It is seen that reasonably good agreement is obtained. These theory-experiment comparisons thus provide strong support to the understanding of the ER mechanism as the result of induced polarization, made quantitatively predictable through the effective dielectric constant formulation with the Bergman–Milton spectral representation.

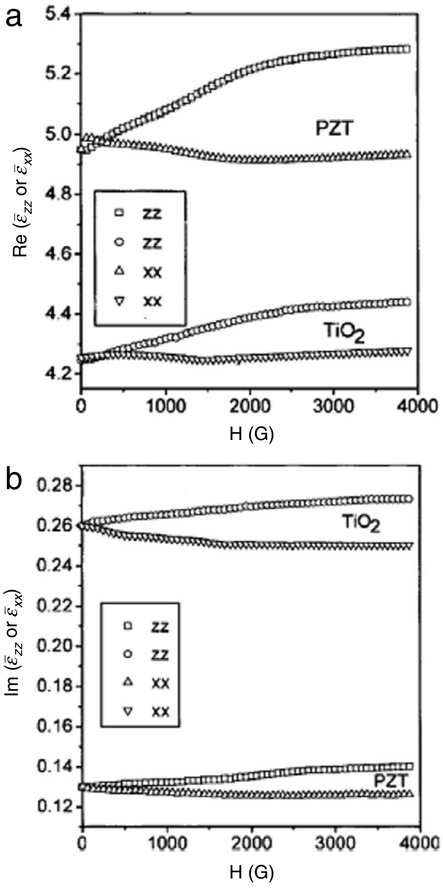

Fig. 10. Dependences of real (a) and imaginary (b) parts of the dielectric constant on applied magnetic field strength. Here the volume fraction is 0.27, and the frequency of the LCR meter is fixed at 1 kHz.

4. The giant electrorheological effect

There is a basic difference between the maximum (dimensionless) electric susceptibility of a collection of permanent dipoles and a system of polarizable particles, which may be heuristically quantified as follows. For a polarizable particle, the polarizability $\alpha = \beta a^3$ has a maximum value given by $\alpha = a^3(\beta = 1)$, attained by setting $\varepsilon_s \to \infty$ (here we exclude from our consideration negative ε_s values). If we take the largest possible number density of the polarizable particles, $N = (4\pi a^3/3)^{-1}$, then the dimensionless $\chi = N\alpha$ has the maximum value of $3/4\pi = 0.239$. In contrast,

Table 2
Experimental and theoretical results of the real and imaginary parts of ER fluid dielectric constants measured along the z and x directions for the random and structured cases.

Structure		Theory		Experiment	
		Re ($\bar{\varepsilon}$)	Im ($\bar{\varepsilon}$)	Re ($\bar{\varepsilon}$)	Im ($\bar{\varepsilon}$)
Random		Fitted	Fitted	4.95	0.13
PZT coating	*zz*	5.67	0.23	5.29	0.14
	xx	4.75	0.11	4.94	0.12
Random		Fitted	Fitted	4.26	0.26
TiO_2 coating	*zz*	4.56	0.37	4.44	0.28
	xx	4.15	0.23	4.25	0.25

for a collection of molecular dipoles, the polarizability arises from the competition of thermal Brownian motion and the alignment effect of the applied electric field. The standard calculation leads to $\alpha = \mu_0^2/3k_BT$, where μ_0 denotes the molecular dipole moment, k_B the Boltzmann constant, and T the temperature. If we let T be room temperature and μ_0 be one electronic charge separated (from its opposite) by 1 Å, then multiply that by $N = (\text{molecular volume})^{-1}$, we obtain $\chi \sim 4$–50, depending on what we take for the molecular volume. The fact that there can be at least one order of magnitude difference in the maximally achievable values is easy to see. Of course, the molecular dipoles tend to form quadrupolar pairs, hence getting a dense collection of free molecular dipoles is not a simple matter, yet the potential is there.

4.1. *The giant electrorheological (GER) effect — particle structure and behavior*

The study of the effect of water on the ER effect prompted an attempt to fix OH groups on solid particles. While that was not successful, it led to the discovery of urea-coated nanoparticles of barium titanate oxalate ($NH_2CONH_2 \oplus BaTiO(C_2O_4)_2$) which, when dispersed in silicone oil, exhibits ER effect orders of magnitude larger than those based on the induced polarization mechanism, exceeding the upper bound value by a large amount [20]. The GER effect also displays different electric field dependence of the yield stress, as well as the opposite dependence on the size of the particles [21]. Thus the GER fluids represent a new paradigm.

In Fig. 11(a), a TEM picture shows that the structure of the GER particles consists of a ∼50 nm core of barium titanate oxalate, with a 5 nm coating of urea. In Fig. 11(b), an optical microscope image shows the column formation when an electric field was applied. In Fig. 11(c), a TEM picture shows that under an electric field, the coatings of the nanoparticles are significantly deformed, indicating a degree of softness in the coating.

In Fig. 12, the measured yield stress and current density (shown in the inset) is plotted as a function of the applied electric field. A prominent feature is the near-linear dependence of the yield stress on the electric field. In accordance with the earlier discussion, this is only possible if the yield stress arises not from induced polarization, but rather from the saturation polarization of some permanent molecular dipoles, so that in the expression $-\vec{P}_0 \cdot \vec{E}$ the polarization is a constant. The current density dependence on the electric field follows a so-called Poole–Frenkel mechanism, where the current density $\ell n J \propto \sqrt{E}$ is a signature of charging carriers generated through a breakdown of the dipoles under an electric field. Here the $\sqrt{E}$ behavior is a signature of activation barrier lowering by an applied field, for ions held by the *Coulomb potential* of the counterions, i.e., current density is due to the breakdown of the molecular dipoles.

4.2. *A phenomenological model of the GER effect*

The phenomenological GER model is based on the following elements: (1) the molecular dipoles of urea can form aligned dipolar layers in the *contact region* between two coated nanoparticles, under a moderate electric field of 10^6–10^7 V/cm (shown schematically in Fig. 13(a)); (2) the equilibrium contact state is represented by the balance of the (attractive) electrostatic force with the (repulsive) elastic force; (3) the elastic deformation of two coated spheres in contact is given by the Hertzian solution; (4) there is an electric field enhancement effect at the contact region, with an enhancement factor of $\sim 10^2$ (estimated numerically by using the finite element method); (5) the shear stress is defined as the derivative of the total energy with respect to strain (which is just the shear distortion angle); and (6) the area of the contact region decreases under shear, and the yield stress is given by the stress value at the point of separation (zero contact area). This is illustrated schematically in Fig. 13(b). In the phenomenological model, there is only one adjustable parameter, given by the deformation modulus of the coating. It turns out that the value obtained from fitting is ∼0.1 GPa, similar to that for a liquid and agrees with the TEM observation that the coatings seem to be soft.

The predictions of the model are in good agreement with measured results, as seen from the solid lines in Fig. 12. In particular, the linear dependence on the applied electric field is a direct reflection of the surface saturation polarization. Another prediction of the model is that since the effect owes its origin to surface saturation polarization, more surface area (hence smaller particles) would enhance the GER effect. This turns out to be the case, opposite [21] to the observed size scaling behavior of the induced polarization mechanism as described earlier.

How does the surface saturation polarization come about? That is, what are the microscopic elements contributing to the statistical mechanics of the surface-aligned dipolar layers? While the end-to-end interaction between the dipoles are electrostatically favorable, side-to-side interaction between the dipoles is not. Hence to have two layers of aligned dipoles there must be some other contributing factors, such as the external electric field or chemical interactions, that also participate. These issues represent topics currently under active investigation.

5. Onsager principle and the dynamic equations of motion

In this section we start our consideration of dynamics of nano/microparticles suspension under an applied electric field. We would like to derive the hydrodynamic equations of motion for the ER fluid so that efficient numerical simulations are possible. For this purpose, the Onsager principle is perhaps the most useful. The Onsager principle of minimum energy dissipation [29–32] is about the rules governing the optimal paths of deviation and restoration to equilibrium. Similar variational principles were used or developed by Helmholtz [33], Rayleigh [34], Edward and Freed [35], and Doi [36]. As a variational principle, it is useful as an approach for deriving the equations of motion (as well as for the boundary conditions), but not for determining the global dissipative state. The latter is in contrast to the principle of minimum free energy, which is often used to determine the global ground state of matter.

5.1. *Onsager variational principle — statistical mechanical underpinnings*

To see how the principle of minimum energy dissipation arises, it is instructive to use a one-variable example for illustration. Let α be the displacement from equilibrium. In an overdamped dissipative system, the dynamics may be described by the Langevin equation

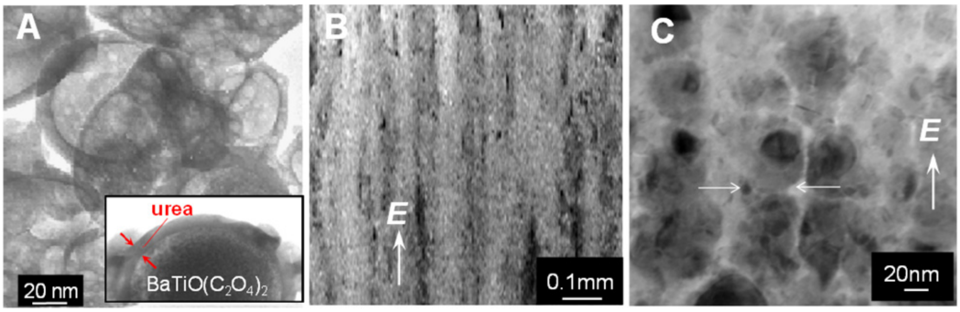

Fig. 11. Images of nanoparticles in GER suspensions. (a) TEM image of coated nanoparticles. Urea coatings are clearly seen. (b) Optical microscope image of a sample prepared in epoxy, solidified under an applied field E of 2 kV mm^{-1}. Columns aligned along the field direction are visible. (c) TEM image of a section of the column shown in (b). The arrows indicate one of the flattened interfaces.

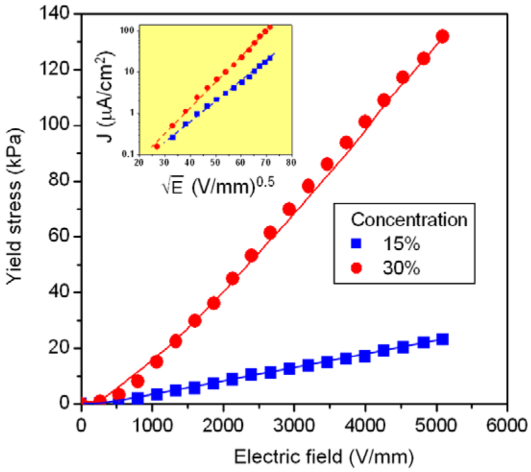

Fig. 12. Static yield stress plotted as a function of applied electric field for two solid concentrations. Symbols denote the experiment; solid lines are theory. Inset: logarithm of the current density J plotted as a function of $\sqrt{E}$. The dashed straight lines serve to delineate the relationship $\ell nJ \sim \sqrt{E}$, indicating the mechanism of activation over the Coulomb barrier (the Poole–Frenkel effect). Note that at a very moderate field of 1000 V mm^{-1} the linear behavior of the yield stress is already established, indicating that a saturated polarization layer contributes to the GER effect.

$$\eta\dot{\alpha} = -\frac{\partial F(\alpha)}{\partial \alpha} + \xi(t), \tag{25}$$

where $\dot{\alpha}$ denotes the rate of change of α, η denotes the friction coefficient, $F(\alpha)$ is the relevant free energy, and $\xi(t)$ is the white noise with a zero mean, satisfying the correlation $\langle \xi(t)\xi(t')\rangle = 2\eta k_B T\delta(t-t')$, where k_B denotes the Boltzmann constant and T the temperature. The left hand side of Eq. (25) is simply the dissipative force, which is balanced by the conservative force plus a stochastic force on the right. With the white noise $\xi(t)$ term on the right hand side of Eq. (25), the dynamics of α are no longer deterministic and its trajectory is best described by a probability density $P(\alpha, t)$ that is governed by the Fokker–Planck equation

$$\frac{\partial P}{\partial t} = D\left[\frac{\partial^2 P}{\partial \alpha^2} + \frac{1}{k_B T}\frac{\partial}{\partial \alpha}\left(\frac{\partial F}{\partial \alpha}P\right)\right], \tag{26}$$

where the diffusion constant D satisfies the Einstein relation $\eta D = k_B T$. It is simple to verify that the *stationary* solution of Eq. (26) is given by the Boltzmann distribution $P_{eq} \propto \exp[-F(\alpha)/k_B T]$, i.e., α likes to be in the state of minimum free energy. The *dynamic* transition probability for α at t to α' at $t + \Delta t$ is given by

$$P(\alpha', t + \Delta t|\alpha, t) = \frac{1}{\sqrt{4\pi D\Delta t}} \exp\left[-\frac{(\alpha' - \alpha)^2}{4D\Delta t}\right] \times \exp\left[-\frac{F(\alpha') - F(\alpha)}{2k_B T}\right], \tag{27}$$

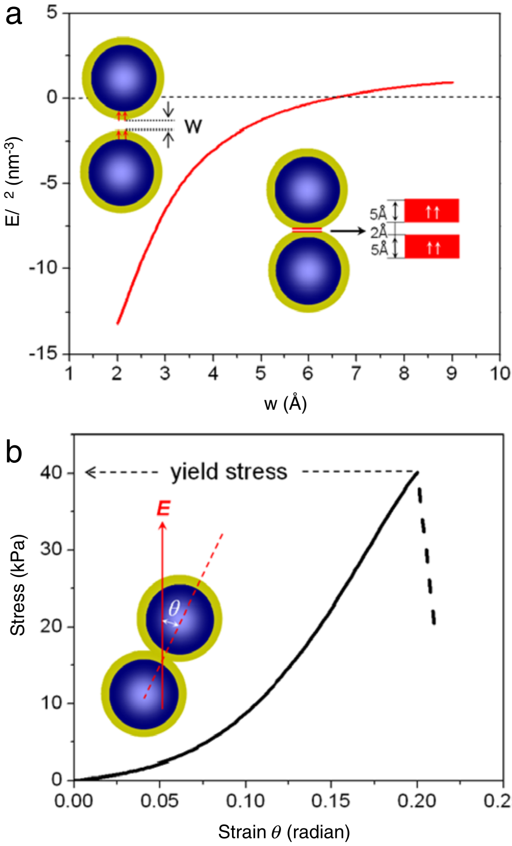

Fig. 13. Illustration of the phenomenological model with calculated results. (a) Upper left: schematic picture of our model, consisting of two coated spheres, each with a 50-nm diameter core and a 5-nm coating (both with $\varepsilon = 60$). The gap, with width w, has $\varepsilon = 2$ (for silicone oil). The solid curve shows the calculated interaction energy divided by μ^2 between two pairs of nearest-neighbour surface dipoles, each with $\mu = 4.6$ Debye and separated laterally by 4.5 Å ($\varepsilon = 1$ between the dipoles), when w increases from 2 Å. In (b), the stress numerically calculated from the finite element method, at an electric field of 2 kV mm^{-1}, is plotted as a function of the strain. The yield stress point corresponds to the point of separation between the two spheres.

for α' in the vicinity of α and small Δt. By using the Einstein relation, the two exponents can be combined:

$$P(\alpha', t + \Delta t|\alpha, t) = \frac{1}{\sqrt{4\pi D\Delta t}} \exp\left[-\frac{A}{2k_B T}\right], \tag{28}$$

where

$$A = \frac{\eta(\alpha' - \alpha)^2}{2\Delta t} + [F(\alpha') - F(\alpha)] \approx \left[\frac{\eta}{2}\dot{\alpha}^2 + \frac{\partial F(\alpha)}{\partial \alpha}\dot{\alpha}\right]\Delta t \tag{29}$$

is the quantity to be *minimized* if we want to maximize the probability of transition with respect to α'. For a small Δt, it is seen that instead of minimizing A with respect to the target state α', the same is achieved by minimizing with respect to the *rate* $\dot{\alpha}$. Indeed, if we carry out the simple minimization on the right hand side of Eq. (29), we obtain the force balance equation

$$\eta\dot{\alpha} = -\frac{\partial F(\alpha)}{\partial\alpha}, \tag{30}$$

i.e., the Langevin equation without the stochastic force term. This is reasonable, since the stochastic force has a zero mean, so Eq. (30) is true on average.

Thus we learn from the above that

(a) there can be a variational functional, of which the quantity A is the one-variable version, which should be minimized with respect to the rates;
(b) the result of such minimization would guarantee the force balance on average; and
(c) the minimization would also yield the equations of motion and the related boundary conditions, which represent the *most probable course of a dissipative process*.

The last statement essentially guarantees that in the statistical sense, the most probable course will be the only dynamic course of action observed macroscopically.

For the general case of multivariables, the variational functional can be simply generalized from Eq. (29) as

$$A = \frac{1}{2}\sum_{i,j}\eta_{ij}\dot{\alpha}_i\dot{\alpha}_j + \sum_{i=1}^{n}\frac{\partial F(\alpha_1,\ldots,\alpha_n)}{\partial\alpha_i}\dot{\alpha}_i, \tag{31}$$

where in the case of α_i's being field variables, the summation should be replaced by integrals, and partial derivatives by functional derivatives. In Eq. (31) the *dissipation coefficient matrix elements* η_{ij} *must be symmetric* with respect to the interchange of the two indices, as shown by Onsager [29,30] based on microscopic reversibility.

5.2. Application of the Onsager principle: Simple examples

Consider the equation of motion for the viscous, incompressible fluid. In that case the viscous dissipation is simply given by

$$R_{vis} = \int \mathrm{d}\vec{r}\left[\frac{\eta}{2}(\partial_i v_j + \partial_j v_i)^2\right], \tag{32}$$

where η is the viscosity coefficient. There is no free energy (time variation) term in this simple example. Hence the variational functional $A = R_{vis}$, which should be minimized with respect to ∂v, together with the incompressibility condition $\nabla\cdot\vec{v} = 0$ (by using the integration by parts, minimizing w.r.t. ∂v is equivalent to minimizing w.r.t. v, which is followed below). That can be accomplished by using the Lagrange multiplier λ. A simple calculation yields

$$-2\eta\int \mathrm{d}\vec{r}\left[\partial_j\left(\partial_j v_i + \partial_i v_j\right)\delta v_i\right] - \int \mathrm{d}\vec{r}\left[\partial_i\lambda\delta v_i\right] = 0, \tag{33}$$

which leads to the Stokes equation

$$-\nabla p + \eta\nabla^2\vec{v} = 0, \tag{34}$$

where we have identified $\lambda = -2p$. This derivation of the Stokes equation from the minimization of viscous dissipation (with the incompressibility constraint) was first recognized by Helmholtz [33]. The inertial effect can be included by requiring momentum balance, in which case we obtain the Navier–Stokes equation

$$\rho[\partial\vec{v}/\partial t + (\vec{v}\cdot\nabla)\vec{v}] = -\nabla p + \eta\nabla^2\vec{v}. \tag{35}$$

There is also a boundary term in the variation of (32), given by the surface integral of the tangential viscous stress $-\eta\partial_n v_\tau$ (here the subscript n denotes the normal component to the boundary, and τ the tangential component), that has been neglected in Eq. (33). This brings into focus the issue of the hydrodynamic boundary condition(s), which is (are) necessary for the solution of the equations of motion. As we know, the non-slip boundary condition is generally the rule at the fluid–solid interface. However, as the solid wall and the fluid are all composed of molecules, albeit with different intermolecular interactions, it is natural to assume the existence of some friction at the fluid–solid interface, with the same form as Eq. (32). Such an assumption does not necessarily rule out the non-slip boundary condition, but may approach it as a limit. We use a discretized version of (32) in order to adapt the viscous dissipation expression to the fluid–solid boundary, with $R_{vis}^{(S)} = \int \mathrm{d}S[(\eta/\Delta z)(\Delta v_x)^2]$, where $\mathrm{d}S = \mathrm{d}\vec{r}/\Delta z$ is the surface differential. Since Δv_x is the relative (tangential) velocity between the fluid layer and the solid boundary, it is precisely what we would call the slip velocity. That directly suggests the form of frictional dissipation rate at the fluid–solid interface to be

$$R_{slip} = \int \mathrm{d}S[\beta(v_\tau^{slip})^2], \tag{36}$$

where the slip coefficient β has the dimension of [viscosity]/[length]. Hence a slip length may be defined as $l_s = \eta/\beta$. The non-slip boundary condition is approached by letting $l_s \to 0$.

If we take the variation of (36) and combine this surface slip dissipation term with the tangential viscous stress obtained from the boundary term in the variation of (32), we obtain the boundary condition

$$\beta v_\tau^{slip} = -\eta\partial_n v_\tau, \tag{37}$$

known as the Navier boundary condition [37], proposed nearly two centuries ago. It is noted that if we let the slip length approach zero so as to obtain the non-slip boundary condition, then the slip velocity must be zero as well in order for the left hand side of Eq. (37) not to diverge. Thus the non-slip boundary condition is a limiting case of Eq. (37).

By extending the Onsager principle to the case of immiscible fluids flow (in which case one must include the free energy time variation term, arising from the fluid-fluid and fluid–solid interfacial energies), it has been shown that a generalized Navier boundary condition is obtained which resolves the classical problem of the moving contact line [38,39]. Moreover, the resulting continuum hydrodynamics can yield for the first time predictions of flow fields in quantitative agreement with molecular dynamic simulations down to the molecular level [40]. However, since the slip length is generally in the nanometer scale, the non-slip boundary condition can be regarded as an excellent approximation for macroscopic flows.

It follows from the above that the Onsager principle offers a unified framework for the derivation of the hydrodynamic equations of motion as well as the associated boundary conditions, although it does not give the values for the relevant parameters, which are specific to the details of the particular model.

6. Electrorheological fluid dynamics

Many of the ER fluid applications involve flows with moderate to high shear-rates. While the static characteristics of the ER fluids can be studied successfully with the effective dielectric constant formulation, the dynamic behavior of ER fluids can represent a challenging topic. A direct simulation involving a number of discrete, electrically interacting particles would be computationally limited by the particle number [41–47], hence difficult to apply to realistic systems. Bingham fluid [48] is often used for the prediction of ER dynamics, in which the dynamic shear stress τ induced by a Couette flow, for example, is given by the expression $\tau = \tau_0 + \eta\dot{\gamma}$, where η denotes viscosity, $\dot{\gamma}$ the shear rate, and τ_0 the threshold shear stress beyond which the fluid-like behavior is recovered. While the Bingham model clearly captures an essential element of the ER dynamics, it fails to account for the often-observed shear thinning behavior and the sensitivity of ER rheology to electrode configuration(s).

Below we describe a two-phase continuum model for the simulation of ER fluid dynamics [49]. This model arises naturally from the observation that under an electric field, the solid particles phase – separate into two components — a dense column phase and a liquid phase as shown in Fig. 2. In this model the electrical interaction between the solid particles is treated on the basis of (induced) dipole–dipole interaction, valid in the limit of weak ER effect. This is in contrast to the more exact treatment of the static properties through the effective dielectric formalism. By regarding the number density of solid particles as a field variable, we shall derive the equations of motion by using the Onsager variational principle. Results obtained are noted to be in excellent agreement with the experiments on systems with a weak ER effect. In particular, it is shown that the shear-thinning behavior of ER dynamics may be avoided by using a planar, alternate-electrode configuration, which may have positive implications for ER fluid applications.

6.1. Model description

Consider identically-sized solid microspheres of radius a ($=5$ μm in our calculations), dielectric constant ε_s ($=10.0$ in our calculations), and mass m ($=1.2 \times 10^{-9}$g in our calculations) suspended in oil with dielectric constant ε_ℓ ($=2.0$ in our calculations), viscosity η_ℓ ($=10$ cP in our calculations), and density ρ_ℓ ($=0.96$ g/cm^3 in our calculations). Due to the difference between ε_s and ε_ℓ, in the presence of an external field the solid particles will be polarized with an induced dipole moment $\beta a^3\vec{E}_l$ as defined by Eq. (1). Here $\vec{E}_l$ denotes the local electric field, which is the sum of the externally applied electrical field $\vec{E}_{ext}$, plus the field from all the other induced dipoles, both at the position of the microsphere. The accurate knowledge of the latter requires a description of the induced dipole distribution in space, which represents the global self-consistent solution of the problem. To facilitate the construction of the model, we first assume that the point dipole $\vec{p}$ is situated at the center of the microsphere. To prevent microspheres from overlapping in space, we introduce a repulsive interaction potential between any two spheres i and j, situated at $\vec{x}$ and $\vec{y}$, respectively, as

$$\varepsilon_0\left(\frac{a}{|\vec{x}-\vec{y}|}\right)^{12}, \tag{38}$$

where ε_0 is a suitably chosen energy constant. Besides regularizing the dipole–dipole interaction, this repulsive interaction term is noted to also affect the viscosity of the dense colloidal (column) phase. Second, we treat the solid particles collectively by regarding their density $n(\vec{x}) = f_s(\vec{x})(4\pi a^3/3)^{-1}$ as a *field variable*, where $f_s(\vec{x})$ denotes the dimensionless, local volume fraction of solid microspheres. This component of our model is denoted by the "s" component. It is obviously not a solid, but rather a homogenized colloidal (column) phase. We will model the viscosity of this dense colloidal phase as a function of $n(\vec{x})$, fitted to experimental data. This is shown below.

One can write down the total energy for the "s" component, including the interaction between the particles and between the particles and the external field, as a functional of $n(\vec{x})$:

$$\begin{aligned}F[n(\vec{x})] = {} & \frac{1}{2}\int G_{ij}(\vec{x},\vec{y})p_i(\vec{x})n(\vec{x})p_j(\vec{y})n(\vec{y})\mathrm{d}\vec{x}\mathrm{d}\vec{y} \\ & - \int \vec{E}_{ext}(\vec{x})\cdot\vec{p}(\vec{x})n(\vec{x})\mathrm{d}\vec{x} \\ & + \frac{\varepsilon_0}{2}\int\left(\frac{a}{|\vec{x}-\vec{y}|}\right)^{12} n(\vec{x})n(\vec{y})\mathrm{d}\vec{x}\mathrm{d}\vec{y},\end{aligned} \tag{39}$$

where

$$G_{ij}(\vec{x},\vec{y}) = \frac{\vec{\vec{I}}_{i,j}}{|\vec{x}-\vec{y}|^3} - \frac{3(\vec{x}-\vec{y})_i(\vec{x}-\vec{y})_j}{|\vec{x}-\vec{y}|^5} = \vec{\nabla}_i\vec{\nabla}_j\frac{1}{|\vec{x}-\vec{y}|} \tag{40}$$

is the dipole interaction operator, and the Einstein summation convention is followed in Eq. (39), where the repeated indices imply summation. A variation of F with respect to n leads to $\delta F = \int \mu(n)\delta n\mathrm{d}\vec{x}$, where

$$\begin{aligned}\mu[n(\vec{x})] = {} & -\vec{E}_{ext}(\vec{x})\cdot\vec{p}(\vec{x}) + \int G_{ij}(\vec{x},\vec{y})p_i(\vec{x})p_j(\vec{y})n(\vec{y})\mathrm{d}\vec{y} \\ & + \varepsilon_0\int\left(\frac{a}{|\vec{x}-\vec{y}|}\right)^{12} n(\vec{y})\mathrm{d}\vec{y}\end{aligned} \tag{41a}$$

is the chemical potential for the "s" component. It should be noted that the first two terms on the right-hand side of Eq. (41a) may be interpreted as $-\vec{E}_l\cdot\vec{p}$, where

$$[\vec{E}_l(\vec{x})]_i = [\vec{E}_{ext}(\vec{x})]_i - \int G_{ij}(\vec{x},\vec{y})p_j(\vec{y})n(\vec{y})\mathrm{d}\vec{y}. \tag{41b}$$

Since n is a locally conserved variable, there is a continuity equation for n, given by

$$\dot{n} + \nabla\cdot\vec{J} = \frac{\partial n}{\partial t} + V_s\cdot\nabla n + \nabla\cdot\vec{J} = 0, \tag{42}$$

where V_s is the "s" phase velocity, and $\vec{J}$ is a convective-diffusive current density.

Besides the "s" component, the model consists of another "ℓ", or liquid, component, together with a coupling term that characterizes the dissipative coupling between the two components.

Here we first give the complete coupled equations of motion for the two-phase model. Their derivation via the Onsager variational principle will be given in the following section. Besides the continuity equation (42), the coupled equations of motion for the "s" phase and the "ℓ" phase are given by

$$\begin{aligned}\rho_s&\left(\frac{\partial\vec{V}_s}{\partial t} + \vec{V}_s\cdot\nabla\vec{V}_s\right) \\ &= -\nabla p_s + \nabla\cdot\tau^s_{visc} + \nabla\cdot\tau_s + K(\vec{V}_\ell - \vec{V}_s),\end{aligned} \tag{43}$$

$$\rho_\ell\left(\frac{\partial\vec{V}_\ell}{\partial t} + \vec{V}_\ell\cdot\nabla\vec{V}_\ell\right) = -\nabla p_\ell + \nabla\cdot\tau^\ell_{visc} + K(\vec{V}_s - \vec{V}_\ell), \tag{44}$$

with the supplementary incompressibility conditions $\nabla\cdot\vec{V}_{s,\ell} = 0$. It should probably be noted that $\vec{V}_s$ denotes the velocity of the dense colloidal phase, which includes both liquid and solid particles. Since both are incompressible, hence $\nabla\cdot\vec{V}_s = 0$. This is to be distinguished from the averaged velocity of the solid particle density, whose divergence would not be zero. In Eq. (43) $\rho_s = mn(\vec{x}) + (1-f_s)\rho_\ell$ is the local mass density of the "s" phase, p_s and p_ℓ

are the pressures in the two phases, $\nabla\cdot\tau_s$ is the force density arising from the energy functional (39), and $\tau^s_{visc} = \eta_s(\nabla\vec{V}_s + \nabla^T\vec{V}_s)/2$, $\tau^\ell_{visc} = \eta_\ell(\nabla\vec{V}_\ell + \nabla^T\vec{V}_\ell)/2$ are the viscous stresses of the two components [33]. While η_ℓ is just the fluid viscosity, for η_s we use the concentration-dependent colloidal viscosity, to be given later. In Eqs. (43) and (44) K is a constant which characterizes the relative drag force density between the "s" and "ℓ" components, in the linear approximation. Hence if we consider only the Stokes drag of the "s" phase by the fluid, then $K = 9f_s\eta_\ell/2a^2$.

In Eqs. (43) and (44), the two crucial expressions, $\vec{J}$ and $\nabla\cdot\tau_s$, are to be specified. This can be done by using the Onsager principle, together with the forms of Eqs. (43) and (44), as shown below.

6.2. Derivation of the two-phase coupled equations of motion

For the "s" component of the ER fluid, the Onsager variational functional is given by

$$A(\vec{J},\vec{V}_s) = \dot{F} + \Phi, \tag{45}$$

where

$$\begin{aligned}\dot{F} &= \int \mu\frac{\partial n}{\partial t}\mathrm{d}\vec{x} = \int \mu\left(\dot{n} - \vec{V}_s\cdot\nabla n\right)\mathrm{d}\vec{x}\\ &= -\int \mu\left(\nabla\cdot\vec{J} + \vec{V}_s\cdot\nabla n\right)\mathrm{d}\vec{x}\\ &= \int\left(\nabla\mu\cdot\vec{J} + n\nabla\mu\cdot\vec{V}_s\right)\mathrm{d}\vec{x},\end{aligned} \tag{46}$$

and Φ is a quadratic function of rates, given as 1/2 the energy dissipation rate,

$$\Phi = \int\left(\frac{1}{4}\eta_s[\partial_i(\vec{V}_s)_j + \partial_j(\vec{V}_s)_i]^2 + \frac{\gamma}{2n}J^2 + \frac{1}{2}K(\vec{V}_\ell - \vec{V}_s)^2\right)\mathrm{d}\vec{x}, \tag{47}$$

together with the constraint of $\nabla\cdot\vec{V}_s = 0$, which can be implemented by using a Lagrange multiplier λ. In Eq. (46), we have used the integration by parts as well as the incompressibility condition to reach the final desired form. In Eq. (47), γ is a frictional coefficient related to the convective-diffusive current's dissipation. The form of the convective-diffusive dissipation can be simply obtained by realizing that $\vec{J} = n\vec{V}_d$, where $\vec{V}_d$ denotes the drift velocity. The dissipative force acting on a single microsphere is $\gamma\vec{V}_d$. Hence the force density is given by $n\gamma\vec{V}_d$, and the energy dissipation rate per unit volume is $n\gamma V_d^2 = \gamma J^2/n$. Taking into account the factor of 1/2 leads directly to the expression shown in Eq. (47). The other two terms of Φ are simply the well-known viscous dissipation and the dissipation caused by the friction between the two components. Minimization of the variational functional with respects to the rates $(\vec{J},\vec{V}_s)$ leads to the desired expression for $\vec{J}$ and the Stokes equation for the "s" component. That is,

$$\vec{J} = -\frac{n}{\gamma}\nabla\mu, \tag{48}$$

and

$$0 = -\nabla p_s + \nabla\cdot\tau^s_{visc} + n\nabla\mu + K(\vec{V}_\ell - \vec{V}_s), \tag{49}$$

where $\lambda = -2p_s$. A comparison of the right-hand sides of Eqs. (49) and (43) leads to the conclusion that $\nabla\cdot\tau_s = n\nabla\mu$. When the inertial effects are not negligible, momentum balance requires the left-hand side of Eq. (49) be replaced by $\rho_s\dot{\vec{V}}_s$, which is precisely Eq. (43).

For the frictional coefficient γ, we propose the Stokes drag form $\gamma = 6\pi\eta_s a$, where it is noted that the viscosity used is that of the effective colloidal viscosity of the "s" component, owing to the (hard core repulsive) interaction between the different microspheres that would determine the drift velocity of a microsphere inside the "s" component. This effective viscosity has been a topic of extensive study both theoretically and experimentally. When the solid particle density is lower than $f_s \leq 0.55$, Pade approximants [50] can be used to represent viscosity variation with f_s. In the lowest order, the viscosity can be written as $\eta_s/\eta_\ell = 1 + \frac{5}{2}f_s + \mathrm{O}\left(f_s^2\right)$. For f_s near the random close pack fraction $f_s^{\max} = 0.698$, experimental results [51] showed an exponential divergence: $\eta_s/\eta_\ell \propto \exp\left[0.6/(f_s^{\max} - f_s)\right]$. In order to cover both the lower and higher ends of the solid density, we have matched the Pade approximation at a lower volume fraction, $f_s \leq 0.45$, and exponential divergence at higher volume fractions $f_s \geq 0.45$. Fig. 14 shows the matched relation. For Eq. (44), which is much simpler than Eq. (43), an almost identical application of the Onsager principle would lead to the desired result.

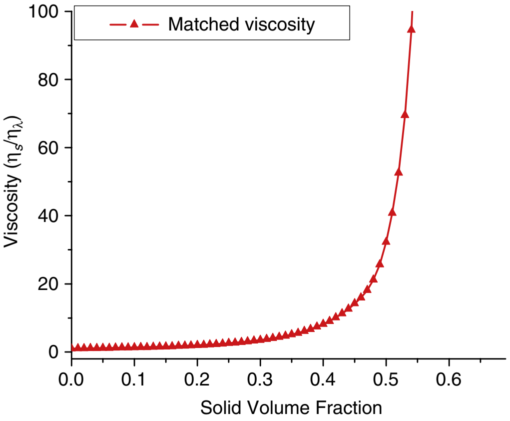

Fig. 14. The "s" component viscosity variation with the solid particles volume fraction. The curve shows the matched variation through the whole range of solid densities.

7. Model predictions and comparison with experiments

Numerical solution of the above scheme consists of two main elements that underlie the dynamics of ER fluids: coupled hydrodynamics of the two components, together with the electrical interactions. The geometry used is that of a channel formed by two plates, parallel to the xy plane, separated by a distance Z_0 (=650 μm in our calculations). The channel is filled with ER fluid. A periodic boundary condition is imposed on the calculational sample boundaries along the x direction. Along the y direction the sample is treated as one particle thick. A non-slip boundary condition is used at the fluid–solid interfaces. This is because the small amount of slip will not alter the main conclusions of the model. The upper plate is assumed to be either moving at a constant speed along the x direction, or moved with some incremental distance along the x direction after the electric field is applied.

7.1. Numerical implementation

The electrical element of the problem enters through the local electric field $[\vec{E}_l(\vec{x})]_i = [\vec{E}_{ext}(\vec{x})]_i - \int G_{ij}(\vec{x},\vec{y})p_j(\vec{y})n(\vec{y})\mathrm{d}\vec{y}$, and Eq. (1) (with the local electric field). Here $\vec{E}_{ext} = -\nabla\phi$, ϕ being the solution of the Laplace equation $\nabla\bar{\varepsilon}(\vec{x})\nabla\phi = 0$, with the local effective dielectric constant $\bar{\varepsilon}$ obtained from the Maxwell–Garnett equation

$$\frac{\bar{\varepsilon}(\vec{x}) - \varepsilon_\ell}{\bar{\varepsilon}(\vec{x}) + 2\varepsilon_\ell} = f_s(\vec{x})\frac{\varepsilon_s - \varepsilon_\ell}{\varepsilon_s + 2\varepsilon_\ell}. \tag{50}$$

The Laplace equation can be solved by specifying the electrode configuration, which can be either the usual condition of constant potentials at the upper and lower plates, or the interdigitated electrodes (shown below). An initial configuration of $n(\vec{x})$ (or $f_s(\vec{x})$) needs to be specified in order to start the solution process. Then $\vec{p}(\vec{x})$ is calculated by initially letting $\vec{E}_l = \vec{E}_{ext}$ in Eq. (1). Once it is obtained, the values are used to obtain a new value for $\vec{E}_l$, which is then used in Eq. (1) to obtain a new $\vec{p}(\vec{x})$, etc, until consistency is achieved. A few iterations suffice.

Numerically, we solve the 2D problem (variations only along x and z directions) by using finite difference with spectral differentiation along the x direction, and explicit in time. Starting from a random initial configuration of $n(\vec{x})$, we first apply the external potential to the problem, and with the local field (and thus $\vec{p}(\vec{x})$ through Eq. (1)) obtained as described above, $n(\vec{x})$ is updated through Eqs. (42) and (48). The updated $n(\vec{x})$ is used to calculated $\bar{\varepsilon}\left(\vec{x}\right)$ through Eq. (50), and the process is iterated till consistency. Thus starting from a random configuration, it is easy to see the formation of chain-like columns in the "s" component when the external field is applied (see below). This is the intuitively desired consequence of an external field, as required by energetics.

The boundary condition of a moving upper plate (or the incremental displacement) is then applied, and the coupled hydrodynamic equations (43) and (44), together with the continuity equation (42), are solved with the incompressibility conditions. The boundary conditions for both $\vec{V}_s$ and $\vec{V}_\ell$ are the non-slip conditions for the tangential components at the upper and lower solid boundaries, and zero normal components. For n, the boundary condition is that the normal component of the convective-diffusive current density $\vec{J}$ be zero at the solid boundaries. By time-stepping forward the solution, at each time step iterating the electrical solution to insure that consistency is achieved in $n(\vec{x})$, we obtain the time evolution of the ER dynamics.

The solution of the Navier–Stokes equation is carried out by using the finite difference scheme, with the pressure-Poisson scheme that is relatively standard.

7.2. Predictions and experimental verifications

In Fig. 15(a), we show that for an electric field applied across two parallel electrodes, the model can reproduce the ER shear elastic behavior up to a critical strain associated with the static yield stress, beyond which the fluid behavior emerges [49]. The shear elasticity is the result of column formation as seen in the inset to Fig. 15(a). Thus this dynamic model can recover some of the static characteristics, in contrast to the Bingham model, for example.

When the top plate is moved at a constant speed relative to the bottom plate to generate a Couette flow, the resulting shear stress experienced on the top plate is plotted as a function of time in the inset to Fig. 15(b). Fluctuations are seen which reflect the breaking and re-attachment of the columns. The time-averaged stress is plotted as a function of shear rate in Fig. 15(b). The behavior is very similar to the Bingham fluid at low shear rates, with an extrapolated dynamic yield stress that is ~30% lower than the static yield stress shown in Fig. 15(a).

Experiments were done in the Poiseuille flow configuration, with different electrode configurations (see insets to Figs. 16 and 17). The ER fluid was prepared by dispersing molecular sieve particles (product type: 3A 1/16, 5 μm in diameter, provided by Nacalai Tesque Inc., Japan) into the silicone oil with a particle concentration of 11.5 vol.%. The prepared ER fluid was baked at 120 °C for one hour to remove any moisture. Tensile machine (MTS SINTECH 10/D Frame Specification) was used for the ER effect measurements, carried out with flow rates varying from

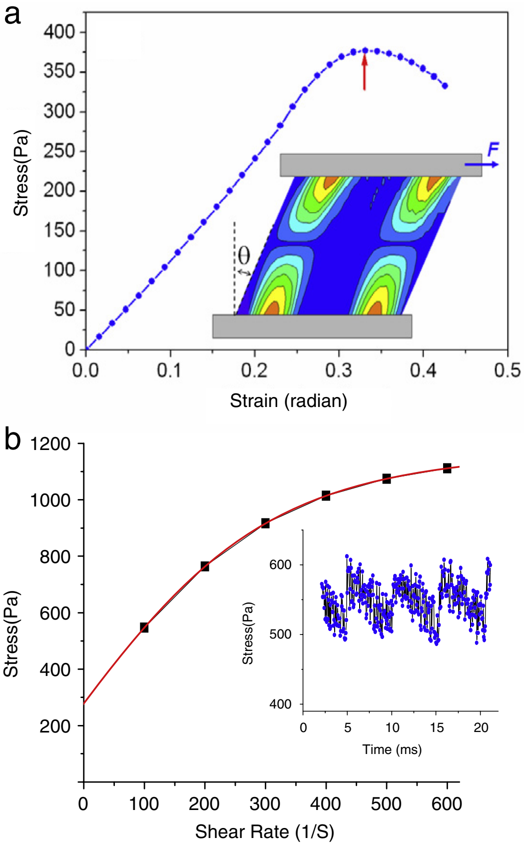

Fig. 15. (a) Calculated shear stress plotted as a function of strain (the angle θ) under an electric field of 2 kV/mm. The cell is 650 μm by 650 μm by $2a$ (y direction), with periodic boundary condition along the shearing direction x. To facilitate the formation of columns under an electric field, the initial density is given by $n_o + \delta n \cdot \cos(kx)$. The inset shows the breaking of the columns at around the yield stress point. Here, red color (light) indicates a high value of n and blue (dark) a low value. The static yield stress is 374 Pa in this case. (b) Calculated (averaged) dynamic shear stress under the Couette flow condition for the same cell as in (a). By extrapolating to the zero shear rate, the dynamic yield stress is found to be 278 Pa. The inset shows the stress fluctuations at a shear rate of 100 s^{-1}. Here $a = 5$ μm, $m = 1.2 \times 10^{-9}$ g, $\varepsilon_s = 10$, $\varepsilon_\ell = 2$, $\eta_\ell = 10$ cp, $\rho_\ell = 0.96$ g/cm^3 and overall $f_s = 30\%$. The zero-field shear stress is very small, hence the behavior shown can be taken to be that for the ER effect only.

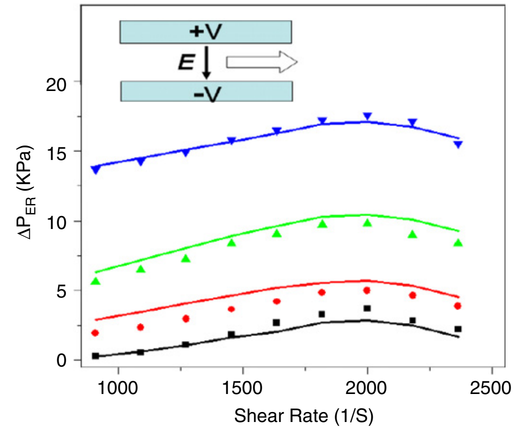

Fig. 16. The (time-averaged) pressure difference due to the ER effect $\Delta P_{ER} = \Delta P_{meas} - \Delta P_{visc}$, plotted as a function of shear rate for the electrode configuration (with a gap of 1 mm) shown in the inset. The symbols and lines represent the experimental and our theoretical results, respectively. From bottom to top: applied electric field is 1 kV/mm, 2 kV/mm, 3 kV/mm and 4 kV/mm. At 1 kV/mm, the pressure difference is very small at low shear rates. Here $a = 2.5$ μm, $m = 1.2 \times 10^{-10}$ g, $\varepsilon_s = 2.9$, $\varepsilon_\ell = 2$, $\eta_\ell = 50$ cp, $\rho_\ell = 0.96$ g/cm^3 and overall $f_s = 11.5\%$.

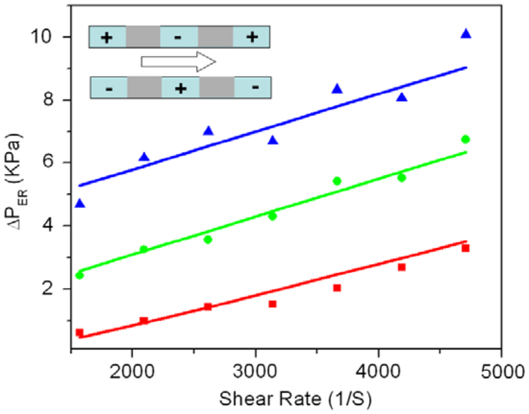

Fig. 17. The pressure difference due to the ER effect $\Delta P_{ER} = \Delta P_{meas} - \Delta P_{visc}$, plotted as a function of shear rate for the planar, alternate electrode configuration. The symbols and lines represent the experimental and our theoretical results. From bottom to top are electrical field equal to 1 kV/mm,1.5 kV/mm and 2 kV/mm. The parameter values used in the calculations are the same as that in Fig. 2.

0.05–150 mm/min through a constriction formed by two parallel plates with a width of 1 cm, length 4 cm and separated by a 1 mm gap. The force on the piston of the cell was measured by a force gauge and recorded with a software package. The resulting pressure difference on two ends of the constriction can be easily obtained from the time-averaged force. A DC power supply (SPELLMAN SL300) provided high voltages applied to the ER fluids.

As mentioned in Section 2.1, when the ER fluid has some finite conductivity, usually involving the transport of ions, then such conductivity would define a time scale τ beyond which the applied voltage will be significantly screened, owing to the migration of the ions to the electrodes. Here, however, in the experiment the ER fluid transit time through the electrode region is 0.04 s at the (lowest) shear rate of 1000 s^{-1}. This is $\sim$20 times smaller than the $\tau = 0.8$ s set by the conductivity of the ER particles.

In Fig. 16, it is seen that for electric field applied across the two parallel plates, there is clearly a shear-thinning behavior at high shear rates. Our simulation results are qualitatively consistent with those presented in [6,52]. Here the shear rate is calculated from the experimental flow rate as $D^{-1}\int_0^D |\partial V(z)/\partial z| \mathrm{d}z$, where D is the distance between the two electrodes and $V(z)$ the calculated velocity profile that matches the flow rate.

There is a simple explanation to the shear-thinning phenomenon based on the fact that since it is the electric field that holds the solid particles together to form the columns, the "adhesive force" for the column formation is necessarily along the field direction z. Initially, when the shear rate is small, the shear stress should increase with the shear rate, since it takes a larger force to break the column within a shorter time. However, as the shear rate increases, the steady-state tilting of the columns as seen in Fig. 15(a) becomes more pronounced. Hence the adhesive force decreases as a cosine of the tilting angle. This leads to the shear thinning as observed. The solid lines are the theory predictions. It is seen that the agreement is excellent. As the theoretical yield stress follows a strictly E^2 variation, the experimental results are seen to be in general agreement with this trend.

An alternative design involving the use of inter-digitated electrodes (inset to Fig. 17) would mean that the applied electric field can have a significant component parallel to the shearing direction. Fig. 17 shows the measured (symbols) and calculated (solid lines) results, up to a high shear rate of 4700/s. The shear thinning effect no longer occurs, seen to be correctly predicted by our continuum model with no adjustable parameters.

8. Concluding remarks

Research on the ER effect is at a stage where both basic and applied aspects present open challenges. In the basic scientific aspect, both the microscopic GER mechanism, as well as the continuous improvement in the ER materials in general, are to be further explored. In the applied aspect, the potential of active mechanical devices, from active dampers to ER clutches and brakes, as well as many other active "smart" devices, remain to be commercially realized. It is thus an exciting prospect to contemplate the future in which ER research can provide an inroad to our understanding of molecular-scale response to moderate external electric fields on the one hand, and to the realization of many active mechanical devices on the other.

Acknowledgements

The authors wish to acknowledge the contributions of W.Y. Tam, M. Loy, H.R. Ma, Jianwei Zhang, Chun Liu, C.T. Chan, N. Wang, and Xiuqing Gong for the works reviewed in this article. Thanks are also owed to Tiezheng Qian and Xiaoping Wang for the many helpful discussions on the Onsager principle.

P.S. especially wishes to thank the von Karman Institute and the KITPC, which supported the lectures that served as the basis of this review article.

References

[1] W.M. Winslow, J. Appl. Phys. 20 (1949) 1137.
[2] W.A. Bullough (Ed.), Electrorheological Fluids, Magnetorheological Suspensions and Associated Technology, Proceedings of the 5th International Conference, World Scientific, Singapore, 1996.
[3] M. Nakano, K. Koyama (Eds.), Electrorheological Fluids, Magnetorheological Suspensions and their Applications, Proceedings of the 6th International Conference, World Scientific, Singapore, 1999.
[4] D.G. Klingenberg, F.V. Swol, C.F. Zukoski, J. Chem. Phys. 91 (1989) 7888.
[5] Y. Chen, A.E. Sprecher, H. Conrad, J. Appl. Phys. 70 (1991) 6796.
[6] T.C. Halsey, Science 258 (1992) 762.
[7] R. Tao, J.M. Sun, Phys. Rev. Lett. 67 (1991) 398.
[8] L.C. Davis, Appl. Phys. Lett. 60 (1992) 319.
[9] L.C. Davis, J. Appl. Phys. 72 (1992) 1334.
[10] T.J. Chen, R.N. Zitter, R. Tao, Phys. Rev. Lett. 68 (1992) 2555.
[11] Y. Chen, H. Conrad, Int. J. Modern Phys. B 8 (1994) 2895.
[12] H. Conrad, A.F. Sprecher, J. Statist. Phys. 64 (1994) 1073.
[13] H.R. Ma, W.J. Wen, W.Y. Tam, P. Sheng, Phys. Rev. Lett. 77 (1996) 2499.
[14] W.Y. Tam, G.H. Yi, W.J. Wen, H.R. Ma, M.M.T. Loy, P. Sheng, Phys. Rev. Lett. 78 (1997) 2987.
[15] W.J. Wen, N. Wang, H.R. Ma, Z.F. Lin, W.Y. Tam, C.T. Chan, P. Sheng, Phys. Rev. Lett. 82 (1999) 4248.
[16] W.J. Wen, H.R. Ma, W.Y. Tam, P. Sheng, Phys. Rev. E 55 (1997) R1294.
[17] Z.W. Wang, H.P. Fang, Z.F. Lin, L.W. Zhou, Phys. Rev. E 61 (2000) 6837.
[18] H.J. Choi, M.S. Cho, J.W. Kim, C.A. Kim, M.S. John, Appl. Phys. Lett. 78 (2001) 3806.
[19] H. Ma, W. Wen, W.Y. Tam, P. Sheng, Adv. Phys. 52 (2003) 343.
[20] W. Wen, X. Huang, S. Yang, K. Lu, P. Sheng, Nature Materials 2 (2003) 727.
[21] W. Wen, X. Huang, P. Sheng, Appl. Phys. Lett. 85 (2004) 299.
[22] X. Huang, W. Wen, S. Yang, P. Sheng, Solid State Commun. 139 (2006) 581.
[23] Graeme W. Milton, The Theory of Composites, Cambridge University Press, Cambridge, UK, 2002.
[24] D.J. Bergman, Phys. Rev. B 19 (1979) 2359.
[25] D.J. Bergman, Ann. Phys. 138 (1982) 78.
[26] G.W. Milton, J. Appl. Phys. 52 (1980) 5286.
[27] G.W. Milton, Appl. Phys. A 26 (1981) 1207.
[28] D.J. Bergman, D. Stroud (Eds.), Solid State Physics, vol. 46, Academic Press, 1992.
[29] L. Onsager, Phys. Rev. 37 (1931) 405.
[30] L. Onsager, Phys. Rev. 38 (1931) 2265.
[31] L. Onsager, S. Machlup, Phys. Rev. 91 (1953) 1505.
[32] L.D. Landau, E.M. Lifshitz, Statistical Physics, 2 edition, Addison-Wesley Publishing Co., London, 1969.
[33] G.K. Batchelor, An Introduction to Fluid Dynamics, Cambridge University Press, Cambridge, UK, 1967.
[34] Lord Rayleigh, Proc. Math. Soc. Lond. 4 (1873) 357.
[35] S.F. Edward, K.F. Freed, J. Chem. Phys. 61 (1974) 1189.
[36] M. Doi, J. Chem. Phys. 79 (1983) 5080.
[37] C.L.M.H. Navier, Mem. L'Acad. R. Sci. l'Inst. France 6 (1823) 389.
[38] T. Qian, X.-P. Wang, P. Sheng, J. Fluid. Mech. 564 (2006) 333.
[39] T. Qian, C. Qiu, P. Sheng, J. Fluid Mech. 611 (2008) 333.
[40] T. Qian, X.P. Wang, P. Sheng, Phys. Rev. E 68 (2003) 016306.
[41] R.T. Bonnecaze, J.F. Brady, J. Rheol. 36 (1992) 73.
[42] R.T. Bonnecaze, J.F. Brady, J. Chem. Phys. 96 (1992) 2183.
[43] D.J. Klingenberg, F.V. Swol, C.F. Zukoski, J. Chem. Phys. 91 (1989) 7888.
[44] D.J. Klingenberg, F.V. Swol, C.F. Zukoski, J. Chem. Phys. 94 (1991) 6160.
[45] D.J. Klingenberg, J. Rheol. 37 (1993) 199.

[46] D.J. Klingenberg, C.F. Zukoski, J.C. Hill, J. Appl. Phys. 73 (1993) 4644.
[47] K.C. Hass, Phys. Rev. E 47 (1993) 3362.
[48] A.H. Skelland, Non-Newtonian Flow and Heat Transfer, John Wiley, New York, 1967.
[49] J. Zhang, X. Gong, C. Liu, W. Wen, P. Sheng, Phys. Rev. Lett. 101 (2008) 194503.
[50] R. Verberg, I. de Schepper, E. Cohen, Phys. Rev. E 55 (1997) 3143.
[51] Z. Cheng, J. Zhu, P. Chaikin, S. Phan, W. Russell, Phys. Rev. E 65 (2002) 041405.
[52] J. Martin, J. Odinek, T. Halsey, R. Kamien, Phys. Rev. E 57 (1998) 756.